Lattice QCD with two-flavor Wilson fermions for static-quark free energies and quark number densities at finite chemical potential

髙橋, 純一

https://doi.org/10.15017/1654645

出版情報：九州大学, 2015, 博士（理学）, 課程博士
バージョン：

Lattice QCD with two-flavor Wilson fermions for static-quark free energies and quark number densities at finite chemical potential

Junichi Takahashi

Theoretical Nuclear Physics, Department of Physics

Graduate School of Science, Kyushu University

744, Motooka, Nishi-ku, Fukuoka 819-0395, Japan

Abstract

Quantum chromodynamics (QCD) is the theory for describing strong interaction working between quarks and gluons. It is a representative theory with asymptotic freedom. Therefore, QCD is considered to have several different phases at finite temperature (T) and/or finite quark-number chemical potential (μ). In fact, in the low-T and small-μ region, the system is in the hadron phase where quarks are confined in hadrons and the spontaneous breaking of chiral symmetry takes place. In the high-T region, we expect from asymptotic freedom that the system is in the quark-gluon plasma phase where chiral symmetry is restored and quarks are deconfined. In the low-T and large-μ region, it is considered that there exists the color superconductor phase in which two quarks form a Cooper pair through attractive quark-quark interactions. Unraveling the phase diagram in the T-μ plane is one of the most important subjects in hadron physics and its related fields.

There are many fascinating subjects on QCD at finite μ; for example, beam energy scan experiments for the QCD phase diagram, properties of nuclear matter, the inner-core structure of compact stars, and so on. Lattice QCD (LQCD) is the first-principle calculation of QCD and hence the most powerful method for studying QCD. However, LQCD has the notorious sign problem at finite μ. Several methods were proposed so far to avoid the sign problem, but these are still far from perfection.

In this dissertation, we investigate the static-quark free energy and the quark number density at finite T and μ by making LQCD at imaginary μ where LQCD has no sing problem and extrapolating the results to real μ. This is the important first step toward our final goal of understanding the QCD phase diagram perfectly. LQCD simulations are performed with the clover improved two-flavor Wilson quark action and the renormalization-group-improved Iwasaki gauge action at imaginary μ ($\equiv i\mu_{\rm I}$). LQCD results at imaginary μ are extrapolated to the real-μ region by assuming func-

tion forms. First, we study μ dependence of the static-quark free energies in various color channels. The static-quark free energies are expanded up to the fourth order of $i\theta(\equiv i\mu_{\rm I}/T)$, and effects of the fourth-order coefficients are investigated. Second, we extract the color-Debye screening mass from LQCD results of static-quark free energies in order to study color-screening effects at finite μ. The color-Debye screening mass is compared with the prediction of hard-thermal-loop perturbation theory at both imaginary and real μ. Third, we study μ dependence of the quark number density. The density obtained at imaginary μ is extrapolated to real μ by assuming a Fourier series for the confinement region and a polynomial series for the deconfinement region. The upper bound of the reliable extrapolated region is estimated for each T in the deconfinement region. Finally, we examine whether T dependence of nucleon and Δ-resonance masses can be estimated from the LQCD results on the quark number density at imaginary μ by using the hadron resonance gas model. It is significant to study μ dependence of the static-quark free energy and the quark number density by using the present imaginary-μ approach from the viewpoint of not only physical interest but also consistency check between different methods and quark actions.

This dissertation is based on the following two published papers:

- Color screening potential at finite density in two-flavor lattice QCD with Wilson fermions,
  J. Takahashi, K. Nagata, T. Saito, A. Nakamura, T. Sasaki, H. Kouno, and M. Yahiro, Phys. Rev. D 88, 114504 (2013).

- Quark number densities at imaginary chemical potential in $N_f = 2$ lattice QCD with Wilson fermions and its model analyses,
  J. Takahashi, H. Kouno, and M. Yahiro, Phys. Rev. D 91, 014501 (2015).

Contents

List of Figures

List of Tables

Chapter 1

Introduction

First we introduce quantum chromodynamics (QCD) in Sec. 1.1, and explain typical properties of QCD at finite temperature (T) and finite quark-number chemical potential (μ) in Sec. 1.2. It is known that QCD at finite μ has the sign problem that prevents us from doing lattice QCD simulations as the first-principle calculation of QCD. In Sec. 1.3, the sign problem is explained. Some methods were proposed so far to avoid the sign problem. In our study, we takes the analytic continuation from imaginary μ to real μ. We then discuss properties of QCD in the imaginary μ region in Sec. 1.4. Finally we show our strategy for studying QCD at finite μ.

1.1 Hadrons, Quarks, and Quantum Chromodynamics

Hadrons are composite particles made of quarks. These are classified into baryon and meson, where baryons are three-quark bound states and mesons are quark and anti-quark bound states. Typical baryons are nucleons (proton and neutron), and a typical meson is pion as an origin of nucleon force. Hadrons are used to be considered as elementary particles, but many hadrons were discovered by the improvement of experimental techniques, and eventually it was shown by inelastic electron-nucleon scattering experiments that hadrons have intrinsic structures. Quarks were then introduced as constituent particles of hadron and gluons were as the particles that mediate between quarks [1]. The interaction working between quarks is now called "strong interaction".

Dynamics of quarks and gluons is described by quantum chromodynamics (QCD)

that is non-Abelian gauge theory with color $SU(3)$. The Lagrangian density is written by

$$\mathcal{L} = \bar{q}(i\gamma^\mu D_\mu - m)q - \frac{1}{4}F^a_{\mu\nu}F_a^{\mu\nu}, \tag{1.1}$$

where q, $\bar{q}$ and A_μ are quark, anti-quark and gluon fields, respectively, and m is the current quark mass. The operator $D_\mu = \partial_\mu + igA^a_\mu T^a$ is the covariant derivative with the coupling constant g and the generators T^a of $SU(3)$ group, and $F^a_{\mu\nu}$ is the field strength tensor defined by

$$F^a_{\mu\nu} = \partial_\mu A^a_\nu - \partial_\nu A^a_\mu - g f^{abc} A^b_\mu A^c_\nu \tag{1.2}$$

with the structure constant f^{abc}. The Lagrangian density is invariant under the local gauge transformation,

$$q(x) \rightarrow q'(x) = V(x)q(x), \tag{1.3}$$

$$\bar{q}(x) \rightarrow \bar{q}'(x) = \bar{q}(x)V^\dagger(x), \tag{1.4}$$

$$A_\mu(x) \rightarrow A'_\mu(x) = V(x)(A_\mu(x) - (i/g)\partial_\mu)V^\dagger(x), \tag{1.5}$$

for $V(x) = \exp(-i\theta^a(x)T^a) \in SU(3)$.

Six kinds of quarks were discovered so far. The species of quarks is now referred to "flavors": u (up), d (down), s (strange), c (charm), b (bottom), and t (top). The empirical values of current quark masses are tabulated in Table 1.1, where u-, d- and s-quark masses are estimated with the mass-independent subtraction scheme ($\overline{\rm MS}$ scheme) at a scale $\mu \approx 2$GeV, and c-, b- and t-quark masses are running masses in the $\overline{\rm MS}$ scheme. As shown in Table 1.1, c-, b- and t-quark masses are much larger than the typical energy scale of QCD, $\Lambda_{\rm QCD} \sim 200$ MeV. Then these quarks hardly affect low-energy dynamics of our interest. Therefore, c, b and t quarks are neglected in this dissertation.

From the analysis of the perturbative renormalization group method, QCD is found to be the theory that has asymptotic freedom. Since the coupling constant of QCD becomes small at high energy or at short distance, quarks behave as free particles there. Meanwhile, the coupling constant becomes large at low energy or at long distance. We then have to consider QCD nonperturbatively there.

m_{u}	m_{d}	m_{s}	m_{c}	m_{b}	m_{t}
2.3 MeV	4.8 MeV	95 MeV	1.275 GeV	4.18 GeV	160 GeV

Table 1.1: Summary of current quark masses in QCD [2].

1.1.1 Confinement and $\mathbb{Z}_3$ symmetry

One of nonperturbative features of QCD is color confinement. This is the phenomenon that color-charged particles such as quarks are not observed alone. In other words, only color-singlet states are observed as hadrons. The mechanism of color confinement is still not understood perfectly, but it is confirmed numerically with lattice QCD (LQCD) [3].

Now, we consider the pure $SU(N_c)$ gauge limit of QCD for the case of finite T, where N_c is the number of colors. Since the gauge field $A_\mu(\tau, \boldsymbol{x})$ is periodic in the imaginary-time direction, a global gauge-invariant quantity is defined as

$$\Phi(\boldsymbol{x}) \equiv \frac{1}{N_c}\mathrm{tr}_c \mathcal{T} \exp\left[ig\int_0^{1/T} d\tau A_4(\tau, \boldsymbol{x})\right] \equiv \mathrm{tr}_c L(\boldsymbol{x}), \tag{1.6}$$

where $\mathcal{T}$, tr_c and τ represent the time-ordered product, the trace in color space and the imaginary-time variable, respectively. The $\Phi(\boldsymbol{x})$ is called the Polyakov loop operator. Under the gauge transformation that satisfies the periodic boundary condition in the imaginary-time direction,

$$V(1/T, \boldsymbol{x}) = V(0, \boldsymbol{x}), \tag{1.7}$$

the Polyakov loop operator is invariant:

$$\Phi(\boldsymbol{x}) \to \Phi'(\boldsymbol{x}) = \mathrm{tr}_c \left(V(1/T, \boldsymbol{x}) L(\boldsymbol{x}) V^{-1}(0, \boldsymbol{x})\right) = \Phi(\boldsymbol{x}). \tag{1.8}$$

Next, we consider the gauge transformation with the following boundary condition:

$$V(\tau + 1/T, \boldsymbol{x}) = \boldsymbol{z} V(\tau, \boldsymbol{x}), \tag{1.9}$$

with elements $\boldsymbol{z}$ of the center group $\mathbb{Z}_{N_c}$ of $SU(N_c)$,

$$\boldsymbol{z} = e^{2\pi i n/N_c} I \equiv z_n I, \tag{1.10}$$

where i is the imaginary unit, n is an integer and I is the $N_c \times N_c$ unit matrix. This transformation is called "$\mathbb{Z}_{N_c}$ transformation". The pure gauge action is invariant under this $\mathbb{Z}_{N_c}$ transformation. This symmetry is now called $\mathbb{Z}_{N_c}$ symmetry. The Polyakov loop operator is not invariant under the $\mathbb{Z}_{N_c}$ transformation,

$$\Phi(\boldsymbol{x}) \to \Phi'(\boldsymbol{x}) = \boldsymbol{z}\Phi(\boldsymbol{x}), \tag{1.11}$$

except for the case of $\Phi(\boldsymbol{x}) = 0$. It is known that the expectation value $\langle\Phi\rangle$ of $\Phi(\boldsymbol{x})$ is finite at high T, but zero at $T = 0$ [4]. The expectation value $\langle\Phi\rangle$ is called the Polyakov loop and is an order parameter of spontaneous $\mathbb{Z}_{N_c}$ symmetry breaking.

Here, we consider a static quark in strongly interacting matter. The imaginary-time evolution of static quark field ψ is written in the Coulomb gauge condition by

$$\left(i\frac{\partial}{\partial\tau} + gA_4(\tau, \boldsymbol{x})\right)\psi(\tau, \boldsymbol{x}) = 0. \tag{1.12}$$

Solving Eq. (1.12), one can obtain

$$\psi(\beta, \boldsymbol{x}) = L(\boldsymbol{x})\psi(0, \boldsymbol{x}). \tag{1.13}$$

Thus $L(\boldsymbol{x})$ is the operator that propagates a static quark from $\tau = 0$ to $\tau = \beta$. We then consider the free energy F_q of static quark staying at a position $\boldsymbol{x}$ as

$$\begin{aligned}
e^{-\beta F_q} &\equiv \frac{1}{N_c}\sum_{|s\rangle}\langle s|\psi(0,\boldsymbol{x})e^{-\beta H}\psi^\dagger(0,\boldsymbol{x})|s\rangle \Big/ \sum_{|s\rangle}\langle s|e^{-\beta H}|s\rangle \\
&= \frac{1}{N_c}\sum_{|s\rangle}\langle s|e^{-\beta H}\psi(\beta,\boldsymbol{x})\psi^\dagger(0,\boldsymbol{x})|s\rangle \Big/ \sum_{|s\rangle}\langle s|e^{-\beta H}|s\rangle \qquad (1.14) \\
&= \frac{1}{N_c}\sum_{|s\rangle}\langle s|e^{-\beta H}\mathrm{tr}_c\, L(\boldsymbol{x})|s\rangle \Big/ \sum_{|s\rangle}\langle s|e^{-\beta H}|s\rangle \\
&= \frac{\mathrm{Tr}(e^{-\beta H}\Phi(\boldsymbol{x}))}{\mathrm{Tr}(e^{-\beta H})} = \langle\Phi\rangle, \qquad (1.15)
\end{aligned}$$

where $|s\rangle$ is the complete set of Hamiltonian H and Tr represents the trace over all the states of pure gauge theory. Equation (1.15) shows the relation between F_q and $\langle\Phi\rangle$.

In summary, the Polyakov loop $\langle\Phi\rangle$ is an order parameter of the deconfinement phase transition. When $\langle\Phi\rangle = 0$, F_q becomes infinite and then any quark never appears. This is nothing but quark confinement. Meanwhile, F_q becomes finite when $\langle\Phi\rangle \neq 0$. In this situation, quark can appear as an isolated particle, indicating quark deconfinement.

1.1.2 Spontaneous breaking of chiral symmetry

Another nonperturbative feature of QCD is the spontaneous breaking of chiral symmetry. This phenomenon occurs at low energy. As a consequence of the symmetry breaking, nucleon mass is generated. For example, current u- and d-quark masses are too light to explain proton mass $m_{\rm p} \sim 938$ MeV, as shown in Table 1.1. In fact, the main part of proton mass arises from the chiral symmetry breaking.

Now, we consider the fermion part of two-flavor QCD in the massless limit,

$$\mathcal{L}_q = \bar{q} i\gamma^\mu D_\mu q, \tag{1.16}$$

where the quark field q means the flavor doublet spinor,

$$q = \begin{pmatrix} u \\ d \end{pmatrix}. \tag{1.17}$$

The field q can be decomposed into the left- and right-handed parts by the chirality operator γ_5:

$$q_{\rm L} \equiv \frac{1-\gamma_5}{2} q, \quad q_{\rm R} \equiv \frac{1+\gamma_5}{2} q. \tag{1.18}$$

The QCD Lagrangian of Eq. (1.16) is then rewritten into

$$\mathcal{L}_q = \bar{q}_{\rm L} i\gamma^\mu D_\mu q_{\rm L} + \bar{q}_{\rm R} i\gamma^\mu D_\mu q_{\rm R}. \tag{1.19}$$

The Lagrangian (1.19) is invariant under the following phase transformations,

$$q_{\rm L} \to q'_{\rm L} = e^{-i\tau^a \theta^a_{\rm L}} q_{\rm L}, \quad q_{\rm R} \to q'_{\rm R} = e^{-i\tau^a \theta^a_{\rm R}} q_{\rm R} \tag{1.20}$$

for arbitrary parameters $\theta^a_{\rm L,R}$, where τ^0 and τ^i $(i = 1, 2, 3)$ are the 2×2 unit and Pauli matrices, respectively. These transformations are elements of the $U_{\rm L}(2) \otimes U_{\rm R}(2)$ group (the chiral group), and the invariance is called chiral symmetry. The chiral group is decomposed into $U_{\rm V}(1) \otimes U_{\rm A}(1) \otimes SU_{\rm V}(2) \otimes SU_{\rm A}(2)$. $U_{\rm V}(1)$ symmetry is related to the baryon-number conservation, while $U_{\rm A}(1)$ is anomalous in the sense that it is broken by quantum effects. The remainder $SU_A(2)$ is spontaneously broken when the chiral condensate,

$$\langle \bar{q} q \rangle = \langle \bar{q}_{\rm L} q_{\rm R} + \bar{q}_{\rm R} q_{\rm L} \rangle, \tag{1.21}$$

is finite. This spontaneous breaking of chiral symmetry generates massless Nambu-Goldstone bosons, and makes quarks massive effectively. The mass is called "dynamical quark mass". Since the current (bare) quark mass is not zero in the real world, chiral symmetry is broken explicitly but weakly. This makes pion massive, although the mass is much lighter than those of other hadrons.

1.2 QCD at finite temperature and chemical potential

QCD is a representative theory with asymptotic freedom, as seen in Sec. 1.1. Hence, the vacuum is different between high- and low-energy scales [5]. This suggests that there exist some states at finite T and μ. Figure 1.1 shows a schematic picture of QCD phase diagram in T-μ plane. In general, QCD has to be solved nonperturbatively, although the Lagrangian is established. This makes it difficult to determine QCD phase structure. Thus, the phase diagram is still unknown in most of regions.

In the low-T and small-μ region, quarks are confined in hadrons and the vacuum has the chiral symmetry breaking. This phase is called the hadron phase. This phase is dominated by nucleons and pions particularly at low T. The region of $T = \mu = 0$ corresponds to the real world. There are many experimental data on hadrons and nu-

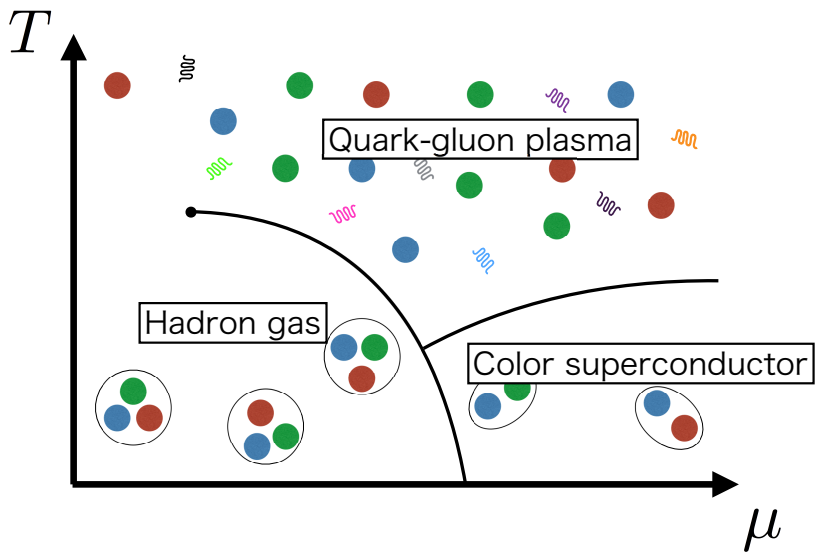

Figure 1.1: Schematic picture of QCD phase diagram on T-μ plane.

clei, and many studies have been made on nuclear force, hadron spectra and hadron structure [6, 7, 8, 9].

In the high-T region, chiral symmetry is restored and quarks are deconfined. We then expect the quark-gluon plasma (QGP) in which quarks and gluons behave as free particles. This phase is called the QGP phase. This is considered to be realized in the early universe. The QGP can be investigated by high-energy collisions of heavy ions such as gold and lead nuclei. In fact, Relativistic Heavy-Ion Collider (RHIC) at Brookhaven National Laboratory recently provided us evidence of QGP [10, 11, 12, 13]. The QGP and the transition between the QGP and hadron phases were also analyzed with LQCD simulations by calculating the Polyakov loop, the chiral condensation [14], and thermodynamic quantities such as the equation of state (EOS) [15, 16, 17, 18].

In the low-T and large-μ region, it is expected that there exists the color superconductor in which two quarks form a Cooper pair through attractive quark-quark interaction in its color antitriplet channel. This phase is called the color superconductor phase. There is a probability that the state exists in the inner core of high-density astronomical objects such as neutron star. The beam energy scan experiments [19, 20] have run in order to research the QCD phase diagram at finite μ, but the experiments do not reach very high densities such as five times the normal-nuclear density

($\rho_0 \sim 0.17$ [fm^{-3}]). LQCD simulations are not feasible here because of the sign problem, as mentioned in Sec. 1.3. Then, any definite result is not obtained yet in this region. This region is still quite unknown.

1.3 Sign problem

There are many interesting topics in QCD at finite μ, but it is not easy to investigate them with LQCD, because of the notorious sign problem. The QCD partition function Z is written by

$$\begin{aligned} Z &= \mathrm{Tr}\left(e^{-(H_{\mathrm{QCD}}-\mu N)/T}\right) \\ &= \int \mathcal{D}A\mathcal{D}\bar{q}\mathcal{D}q \exp\left[-\int_0^{1/T} d\tau \int d^3\boldsymbol{x}\mathcal{L}_{\mathrm{QCD}}\right], \qquad (1.22) \\ \mathcal{L}_{\mathrm{QCD}} &= \mathcal{L}_g + \bar{q}(-i\gamma_\mu D_\mu + m - \mu\gamma_4)q, \qquad (1.23) \end{aligned}$$

in the path integral formulation, where H_{QCD} is the QCD Hamiltonian, N is the quark number, $\mathcal{L}_{\mathrm{QCD}}$ and $\mathcal{L}_g$ are the Lagrangian density of QCD and its gluon part in Euclidean space, respectively, and the gamma matrices and the gauge field are redefined as $\gamma_4 \equiv i\gamma_0$, and $A_4 \equiv iA_0$. After the quark fields are integrated out, Eq. (1.22) becomes

$$\begin{aligned} Z &= \int \mathcal{D}A \det M(\mu) e^{-S_G}, \qquad (1.24) \\ M(\mu) &= -i\gamma_\mu D_\mu + m - \mu\gamma_4, \qquad (1.25) \\ S_G &= \int_0^{1/T} d\tau \int d^3\boldsymbol{x}\mathcal{L}_g. \qquad (1.26) \end{aligned}$$

In actual LQCD simulations, Monte Carlo integrations are carried out with the importance sampling for the gluon field in Eq. (1.24). For the importance sampling, the weight $w = \det M(\mu) e^{-S_G}$ is interpreted as the probability measure. Therefore the weight w should be real. Since the fermion matrix M satisfies the relation

$$M(\mu) = \gamma_5 M^\dagger(-\mu)\gamma_5, \qquad (1.27)$$

the fermion determinant satisfies the relation

$$(\det M(\mu))^* = \det \gamma_5 M(-\mu)\gamma_5 = \det M(-\mu). \tag{1.28}$$

Obviously, the fermion determinant is real at $\mu = 0$, but not at $\mu \neq 0$. Thus, Monte Carlo integrations are difficult at finite μ.

Several methods were proposed so far to avoid the sign problem. The reweighting method [31] is widely applied to LQCD simulations at real μ/T. The basic idea is to generate gauge configurations at $\mu = 0$ and calculate observables multiplied by the reweighting factor defined below. The QCD partition function of Eq. (1.24) can be rewritten into

$$\begin{aligned} Z(\mu) &= \int \mathcal{D}A \det M(0) \frac{\det M(\mu)}{\det M(0)} e^{-S_G} && (1.29) \\ &= Z(0) \left\langle \frac{\det M(\mu)}{\det M(0)} \right\rangle_{\mu=0}, && (1.30) \end{aligned}$$

where $\det M(\mu)/\det M(0)$ is the reweighting factor. Recently, the reweighting procedure with two parameters, called the multi-parameter reweighting, was made in Refs. [32, 33]. Another way is the Taylor expansion method [34, 30, 29] in which the reweighting factor in Eq. (1.29) is expanded with respect to μ/T and observables are calculated for each order of μ/T.

Very recently, the complex Langevin method [40, 41, 42, 43] and the Lefschetz thimble method [44, 45] have been proposed and investigated with great interest as a method for going beyond $\mu/T = 1$. In both the methods, the gauge field $A^a_\mu(\boldsymbol{x})$ is extended into a complex variable. The complex Langevin method is the Langevin method [46] applied to the complex action. Several remarkable results are obtained, but it is not guaranteed mathematically that the converged solution to the complex Langevin equation is exact. The Lefschetz thimble theory is a mathematically well-defined method based on the Morse theory and Witten's idea [47], but its lattice simulations are very difficult.

1.4 Imaginary chemical potential

One of methods to avoid the sign problem is the imaginary-μ approach. When the chemical potential is a purely imaginary number $\mu = i\mu_{\rm I}$, Eq. (1.27) is rewritten into

$$M(i\mu_{\rm I}) = \gamma_5 M^\dagger(i\mu_{\rm I})\gamma_5. \tag{1.31}$$

Using Eq. (1.31), one can find that the fermion determinant is real:

$$(\det M(i\mu_{\rm I}))^* = \det \gamma_5 M(i\mu_{\rm I})\gamma_5 = \det M(i\mu_{\rm I}). \tag{1.32}$$

Thus there is no sign problem at imaginary μ, and hence LQCD simulations become feasible. In order to obtain physical quantities at real μ, we need the extrapolation from imaginary μ to real μ with analytic continuation. The QCD partition function Z is symmetric for charge conjugation $\mathcal{C}$ that corresponds to the transformation $\mu \to -\mu$. Therefore Z is a function of μ^2. Observable $O(T,\mu)$ can be represented by

$$O(T,\mu) = \sum_n c_n(T) \left(\frac{\mu}{T}\right)^n. \tag{1.33}$$

The coefficients $c_n(T)$ are determined from LQCD results at imaginary μ, when the $c_n(T)$ do not change a lot in the vicinity of the phase transition. The analytic continuation can be performed, since LQCD results do not show any singularity at $\mu = 0$.

In the imaginary-μ region, the QCD partition function has a periodicity of $2\pi/3$ in $\theta(\equiv \mu_{\rm I}/T)$. This is called the Roberge-Weiss (RW) periodicity [48]. Here, we consider the $\mathbb{Z}_3$ transformation introduced in Sec. 1.1.1 for QCD with dynamical quarks in the imaginary-μ region. The QCD partition function at finite T and θ is obtained by the replacement $\mu \to i\theta T$ in Eqs. (1.22) and (1.23);

$$Z(T,\theta) = \int \mathcal{D}A\mathcal{D}\bar{q}\mathcal{D}q \exp\left[-\int_0^{1/T} d\tau \int d^3\boldsymbol{x}\mathcal{L}_{\rm QCD}\right], \tag{1.34}$$

$$\mathcal{L}(T,\theta) = \mathcal{L}_g + \bar{q}(-i\gamma_\mu D_\mu + m - i\gamma_4\theta T)q. \tag{1.35}$$

Changing the boundary condition for the quark fields as

$$q(\tau,\boldsymbol{x}) = -e^{i\theta}q(0,\boldsymbol{x}), \tag{1.36}$$

we can eliminate the term $-\bar{q}i\gamma_4\theta Tq$ in Eq. (1.35). Under the $\mathbb{Z}_3$ transformation, the quark field has the new boundary condition,

$$q(\tau, \boldsymbol{x}) = -z_n e^{i\theta} q(0, \boldsymbol{x}) \tag{1.37}$$

for z_n defined by Eq. (1.10), while the QCD action is invariant. The right-hand side of Eq. (1.34) with the boundary condition (1.37) is then $Z(T, \theta + 2\pi n/3)$. Therefore, we conclude that

$$Z(T, \theta) = Z\left(T, \theta + \frac{2\pi n}{3}\right). \tag{1.38}$$

This RW periodicity is true even in the presence of dynamical quarks with finite masses.

The QCD phase diagram in the imaginary μ region can be governed by the RW periodicity. Figure 1.2 shows a schematic picture of QCD phase diagram in T-θ plane. Here, $T_{\rm c}$ denotes the pseudocritical temperature of deconfinement crossover at $\mu = 0$. The dotted line represents the crossover line at finite θ between the confinement and deconfinement regions. The vertical lines starting at the critical endpoint $T = T_{\rm RW}$ correspond to the first-order phase transition between different $\mathbb{Z}_3$ sectors.

1.5 Strategy

Our final goal is to understand the QCD phase diagram. For this purpose, we have to know properties of QGP and the EOS at finite T and μ. As the first step toward our goal, we investigate the static-quark free energy (interactions between a quark and an anti-quark and between two quarks) and the quark number density at finite T and μ by using LQCD with two-flavor Wilson fermions. LQCD has the sign problem at real μ, as seen in Sec. 1.3. Therefore, we take the imaginary-μ approach to avoid the sign problem. At imaginary μ, we can measure observables accurately with LQCD. We then extrapolate the results at imaginary μ to real μ by assuming function forms in order to obtain the static-quark free energy and the quark number density at real μ.

As for the static-quark free energy, the T dependence was investigated by using quenched LQCD [21, 22, 23] and full LQCD with staggered-type [24] and Wilson-

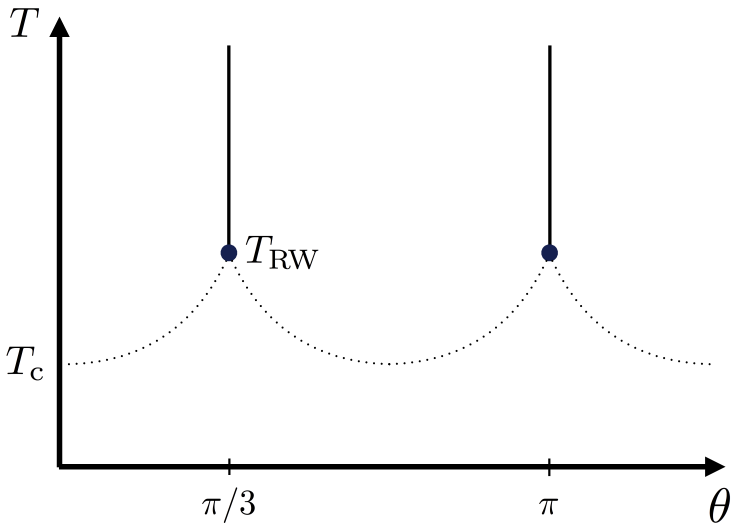

Figure 1.2: Schematic picture of QCD phase diagram on T-θ plane.

type quark actions [25, 26, 27] for $\mu = 0$. For small μ/T, it was studied by the Taylor expansion method with staggered-type [28] and Wilson-type quark actions [29]. The imaginary-μ approach has thus never been applied for the static-quark free energy. Therefore it is significant to study μ dependence of the static-quark free energies with the imaginary-μ approach from the viewpoint not only of physical interest but also of the consistency check between different methods and quark actions.

The quark number density was calculated by the Taylor expansion method with the staggered-type [30] and the Wilson-type quark actions [29] for small μ/T and by the imaginary-μ approach with the staggered-type quark action [35, 36, 37, 38, 39]. It is then also significant to study the quark number density with the imaginary-μ approach based on the Wilson-type quark action from the viewpoint of both physical interest and consistency check.

This dissertation is organized as follows. In Chap. 2, we explain the LQCD action we took. LQCD calculations at finite T have to be done along the line of constant physics. The line of constant physics is then explained in this chapter. In Chap. 3, we investigate μ dependence of the static-quark free energies. In Chap. 4, the quark number density n_q is investigated with LQCD, and the resulting LQCD results are

analyzed with the hadron resonance gas model. Chapter 5 is devoted to a summary.

Chapter 2

Lattice QCD

LQCD is the first-principle calculation for studying properties of QCD such as hadron spectra, thermodynamics of QCD, chiral and deconfinement phase transitions, nuclear force, and so on. In the LQCD formulation, quantization is made by the path integral and is performed by the Monte Carlo integration with the importance sampling. In this chapter, we first explain the LQCD action that we use in this study, particularly for the gauge part in Sec. 2.1 and for the fermion part in Sec. 2.2. LQCD calculations at finite T have to be done along the line of constant physics. The line of constant physics is then explained in Sec. 2.3.

2.1 Lattice gauge action

In the lattice formulation, the gauge field has to be defined properly on a lattice. For this purpose, we first consider the gauge invariance of QCD Lagrangian and the gauge transformation of the quark field. The QCD Lagrangian of Eq. (1.1) is rewritten in Euclidean space as follows:

$$\mathcal{L} = \bar{q}(\gamma_\mu D_\mu + m)q + \frac{1}{4}F^a_{\mu\nu}F^a_{\mu\nu}, \tag{2.1}$$

where the gamma matrices and the gauge field are redefined as $\gamma^0 = \gamma^4$ and $\gamma^i = i\gamma_i\,(i = x, y, z)$ and $A_0 = -iA_4$, respectively. The Lagrangian density is gauge invariant under the gauge transformation of Eqs. (1.3)-(1.5).

The local gauge transformation of the quark field q_n on a lattice point labeled by

an integer-component 4-vector $n = (n_x, n_y, n_z, n_t)$ is written by

$$q_n \rightarrow q'_n = V_n q_n, \tag{2.2}$$

$$\bar{q}_n \rightarrow \bar{q}'_n = \bar{q}_n V_n^\dagger, \tag{2.3}$$

where the physical coordinate is represented by $x = na$ with a the lattice spacing. In order that the lattice quark action is invariant under the local gauge transformations of Eqs. (2.2) and (2.3), the non-local bilinear term $\bar{q}_n q_{n+\hat{\mu}}$ coming from the differential term of QCD action must be gauge invariant, where $\hat{\mu}$ represents a unit vector in μ direction.

In continuum spacetime, a bilinear quantity $\bar{q}(x)q(y)$ is not gauge invariant for $x \neq y$. This problem can be solved by introducing the Schwinger line integral $U(x, y)$ along the ordered path connecting x and y:

$$U(x, y) = \mathcal{P} \exp\left[ig \int_x^y dz_\mu A_\mu(z)\right], \tag{2.4}$$

where $\mathcal{P}$ denotes the path ordered product. The $U(x, y)$ are transformed as

$$U(x, y) \rightarrow U'(x, y) = V(x)U(x, y)V^\dagger(y) \tag{2.5}$$

under the local gauge transformation. Combining Eq. (2.5) with Eqs. (1.3) and (1.4), one can see that $\bar{q}(x)U(x, y)q(y)$ is gauge invariant.

In lattice spacetime, Eq. (2.5) is rewritten into

$$U_{n,\mu} \equiv U(na, na + \hat{\mu}a) = \mathcal{P} \exp\left[ig \int_{na}^{(n+\hat{\mu})a} dz_\mu A_\mu(z)\right]. \tag{2.6}$$

The $U_{n,\mu}$ are called link variables and treated as fundamental variables instead of the gauge field A_μ. The $U_{n,\mu}$ are transformed as

$$U_{n,\mu} \rightarrow U'_{n,\mu} = V_n U_{n,\mu} V^\dagger_{n+\hat{\mu}}. \tag{2.7}$$

Obviously, $\bar{q}_n U_{n,\mu} q_{n+\hat{\mu}}$ is gauge invariant under the lattice gauge transformation of Eqs. (2.2), (2.3) and (2.7).

Not only the quark action but also the gauge action should be gauge invariant

under the lattice gauge transformation. This requires that the product of link variables forms a closed loop in the gauge action composed of link variables only. Wilson [49] proposed a gauge action composed of the smallest closed loops:

$$S_G = \beta \sum_{n,\mu,\nu} \left\{ 1 - \frac{1}{N_c} \mathrm{tr}_c (U_{n,\mu} U_{n+\hat{\mu},\nu} U^\dagger_{n+\hat{\nu},\mu} U^\dagger_{n,\nu}) \right\}, \tag{2.8}$$

for $SU(N_c)$, where $\beta = N_c/g^2$, tr_c stands for the trace over color $SU(N_c)$ indices and $U^\dagger_{n,\mu} = U_{n+\hat{\mu},-\mu}$. This smallest closed loop is called the plaquette and the action (2.8) is named the plaquette action.

In addition to the plaquette action, one can also consider the 1×2-rectangular loop:

$$\begin{aligned} S_G &= \beta \sum_n \left[c_0 \sum_{\mu<\nu;\mu,\nu=1}^{4} W^{1\times 1}_{\mu\nu}(n) + c_1 \sum_{\mu\neq\nu;\mu,\nu=1}^{4} W^{1\times 2}(n) \right], && (2.9) \\ W^{1\times 1}_{\mu\nu}(n) &= \mathrm{tr_c}(U_{n,\mu} U_{n+\hat{\mu},\nu} U^\dagger_{n+\hat{\nu},\mu} U^\dagger_{n,\nu}), && (2.10) \\ W^{1\times 2}(n) &= \mathrm{tr_c}(U_{n,\mu} U_{n+\hat{\mu},\mu} U_{n+2\hat{\mu},\nu} U^\dagger_{n+\hat{\mu}+\hat{\nu},\mu} U^\dagger_{n+\hat{\nu},\mu} U^\dagger_{n,\nu}), && (2.11) \end{aligned}$$

where the coefficients c_0 and c_1 satisfy $c_0 + 8c_1 = 1$. In this dissertation, we take the renormalization-group-improved Iwasaki gauge action [55] in which $c_1 = -0.331$.

2.2 Lattice fermion action

In this section, we consider the fermion action. When the continuum fermion action is simply discretized, there appears a doubling problem, i.e., lattice fermions have extra degrees of freedom. These extra degrees of freedom are called "doublers". One of lattice fermion actions to avoid the doubling problem is the Wilson fermion action [50].

The Wilson fermion action consists of the ordinary fermion action and the Wilson term,

$$S_W = S_F - ar \int d^4x \bar{q}(x) D^2 q(x), \tag{2.12}$$

where S_F is the first term of the right-hand side of Eq. (2.1) and r is the Wilson parameter. Due to the Wilson term, doublers are decoupled from the lattice fermion.

In the lattice formulation, the Wilson fermion action is written as

$$S_W^{(\mathrm{lat.})} = \sum_n \left[\bar{q}_n q_n - \kappa \sum_{\mu=1}^{4} \left\{ \bar{q}_n (r - \gamma_\mu) U_{n,\mu} q_{n+\hat{\mu}} + \bar{q}_n (r + \gamma_\mu) U^\dagger_{n-\hat{\mu},\mu} q_{n-\hat{\mu}} \right\} \right], \quad (2.13)$$

where the hopping parameter κ is defined by

$$\kappa = \frac{1}{8r + 2ma}. \quad (2.14)$$

In this study, we set $r = 1$ and use the values of κ and β on the line of constant physics shown in Sec. 2.3. Obviously, the Wilson fermion action tends to the ordinary fermion action in the limit of $a = 0$, since the Wilson term is proportional to the lattice spacing a. However, it breaks chiral symmetry explicitly even in the chiral limit of $m \to 0$, although the QCD action has chiral symmetry in the chiral limit. According to the Nielsen-Ninomiya theorem [51, 52], any lattice fermion with chiral symmetry has the doubling problem. In other words, the doubling problem can be avoided only when chiral symmetry is explicitly broken. Thus it is an important subject to clarify how the chiral fermion is defined on a lattice.

In this study, we focus our attention on QCD at finite μ. It is then necessary to introduce the chemical potential μ to Eq. (2.13). According to Ref. [53], when μ is introduced by $\pm\mu\bar{q}_n\gamma_4 q_n$ in the lattice fermion action, the energy density diverges quadratically even for free fermion. In order to avoid the divergence, one should consider the exponential form $e^{\pm\mu}$ as

$$\begin{aligned} S_W^{(\mathrm{lat.})}(\kappa,\mu) = \sum_n \bar{q}_n q_n - \kappa \sum_n \sum_{i=1}^{3} \left\{ \bar{q}_n (r - \gamma_i) U_{n,i} q_{n+\hat{i}} + \bar{q}_n (r + \gamma_i) U^\dagger_{n-\hat{i},i} q_{n-\hat{i}} \right\} \\ -\kappa \sum_n \left\{ \bar{q}_n e^{+\mu} (r - \gamma_4) U_{n,4} q_{n+\hat{4}} + \bar{q}_n e^{-\mu} (r + \gamma_4) U^\dagger_{n-\hat{4},4} q_{n-\hat{4}} \right\}, \end{aligned} \quad (2.15)$$

where μ is represented in the lattice unit.

In actual calculations, we take the clover fermion action [54], since $\mathcal{O}(a)$ corrections are made to the Wilson fermion. The part of clover fermion is written by

$$S_C = c_{\mathrm{SW}} \frac{i\kappa r}{2} \sum_n \sum_{\mu,\nu} \bar{q}_n \sigma_{\nu\mu} P_{\mu\nu}(n) q_n, \quad (2.16)$$

where $P_{\mu\nu}(n)$ is the lattice field strength with the standard clover-shaped combination of gauge links,

$$P_{\mu\nu}(n) = \frac{1}{8}\sum_{i=1}^{4}\left[U_i(n) - U_i^\dagger(n)\right], \tag{2.17}$$

$$U_1(n) = U_{n,\mu}U_{n+\hat{\mu},\nu}U^\dagger_{n+\hat{\nu},\mu}U^\dagger_{n,\nu}, \tag{2.18}$$

$$U_2(n) = U_{n,\nu}U^\dagger_{n-\hat{\mu}+\hat{\nu},\mu}U^\dagger_{n-\hat{\mu},\nu}U_{n-\hat{\mu},\mu}, \tag{2.19}$$

$$U_3(n) = U^\dagger_{n-\hat{\mu},\mu}U^\dagger_{n-\hat{\mu}-\hat{\nu},\nu}U_{n-\hat{\mu}-\hat{\nu},\mu}U_{n-\hat{\nu},\nu}, \tag{2.20}$$

$$U_4(n) = U^\dagger_{n-\hat{\nu},\nu}U_{n-\hat{\nu},\mu}U_{n+\hat{\mu}-\hat{\nu},\nu}U^\dagger_{n,\mu}, \tag{2.21}$$

where $\sigma_{\mu\nu} = (i/2)[\gamma_\mu, \gamma_\nu]$ and $c_{\rm SW}$ is the clover coefficient. Here as the value of $c_{\rm SW}$, we adopt a mean-field value calculated in one-loop perturbation theory with the plaquette $W^{1\times1}$ [55], $c_{\rm SW} = (W^{1\times1})^{-3/4} = (1 - 0.8412\beta^{-1})^{-3/4}$.

2.3 Line of constant physics

There are two ways of varying temperature $T = 1/(N_t a)$ in LQCD simulations, where N_t is the lattice size in the temporal extent. One is to change N_t with a fixed. The other is to change the lattice spacing a with N_t fixed. we can easily vary N_t without changing β and κ, but cannot vary the lattice spacing a without changing β and κ, since β and κ are functions of a.

There exist various scales when a is varied. Any bare parameter of theory depends on the regularization. From the viewpoint of scale changing, it is necessary to investigate T dependence of thermodynamic quantities on a lattice. In general, it is difficult to obtain the relation between bare parameters and a. However, the relation can be obtained, when one can find constant values of dimensionless ratio of physical observables, because this ratio should be constant for any lattice spacing a. The constant value of dimensionless ratio of physical observables forms a line, which is called the line of constant physics.

In this study, we take the line of constant physics determined from $m_{\rm PS}/m_{\rm V}$, where $m_{\rm PS}$ and $m_{\rm V}$ are pseudoscalar- and vector-meson mass, respectively. The lines of constant $m_{\rm PS}/m_{\rm V}$ are investigated in Refs. [56, 57, 26], shown in Fig. 2.1. In Fig. 2.1, the solid lines represent lines of constant $m_{\rm PS}/m_{\rm V} = 0.00$, 0.65, 0.70, 0.75, 0.80, 0.85,

0.90, and 0.95, and the dashed lines represent lines of constant $T/T_c = 0.8$, 1.0, 1.2, 1.4, 1.6, 1.8, and 2.0. The explicit values of β and κ used in our studies are shown in Secs. 3.3 and 4.3.

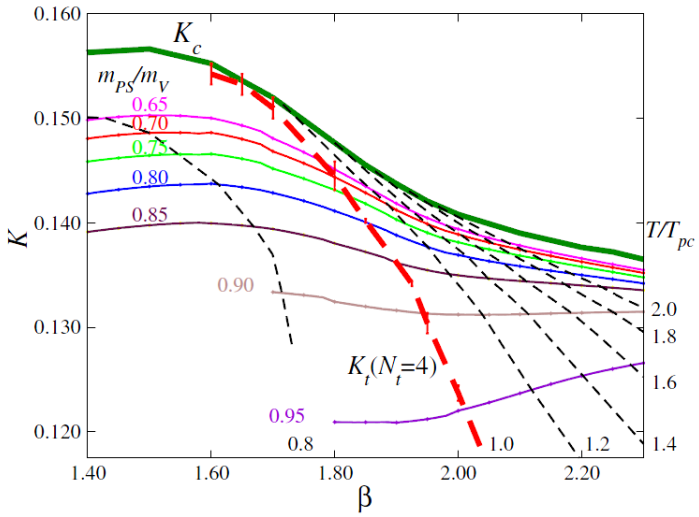

Figure 2.1: Lines of constant $m_{\rm PS}/m_{\rm V}$ and constant T/T_c in β-κ plane for $m_{\rm PS}/m_{\rm V} =$ 0.00, 0.65, 0.70, 0.75, 0.80, 0.85, 0.90 and 0.95 (solid lines) and for $T/T_c = 0.8$, 1.0, 1.2, 1.4, 1.6, 1.8 and 2.0 (dashed lines) on $N_t = 4$ lattices taken from Refs. [56, 57, 26]

Chapter 3

Static-quark free energy

In this chapter, we explain μ dependence of the static-quark free energies (interactions between a quark and an anti-quark and between two quarks). The static-quark free energies are obtained from the correlator of Polyakov loops at imaginary μ by performing LQCD simulations and extrapolating the results to real μ with analytic continuation. LQCD simulations are done on a $16^3 \times 4$ lattice with the clover-improved Wilson fermion action of two flavors and the renormalization-group improved Iwasaki gauge action. We calculate the Taylor expansion coefficients of the static-quark free energies up to the fourth order of $i\mu_{\rm I}/T$. At real μ, the second-order coefficients in the present imaginary-μ approach are consistent with those in the previous Taylor expansion method for the reweighting factor. The fourth-order coefficients are found to be not negligible. In the color-singlet channel, the static-quark free energies have almost the same value at short distances for all the μ we calculated. At long distances, the static-quark free energies tend to twice the single-quark free energy for all the color channels, indicating that the interaction between two static quarks is fully color screened for finite μ. For both imaginary and real μ, the color-singlet $q\bar{q}$ and -antitriplet qq interactions are attractive, whereas the color-octet $q\bar{q}$ and -sextet qq interactions are repulsive. In order to study screening effects of color charges, we fit the static-quark free energy in the color-singlet channel by the screened Coulomb form to obtain the color-Debye screening mass. The mass obtained has stronger μ dependence than the prediction of the hard-thermal-loop perturbation theory at both imaginary and real μ.

3.1 Introduction

At high T, the system is in the QGP that is composed of colored quarks and gluons. This state is considered to be produced by recent relativistic heavy-ion experiments [10, 11, 12, 13]. This may be evidence of the QCD phase transition from the hadronic phase to the QGP phase. In order to obtain clear signals for the transition

from data of the heavy-ion experiments, it is indispensable to make quantitative analyses of QGP with the first principle calculation. LQCD simulation is then one of the most powerful methods.

There are many observables suitable to study thermal properties of QGP and/or phase transitions. For example, the Polyakov loop is an order parameter of the deconfinement phase transition, and the inverse of meson screening mass is the distance beyond which the interactions between hadrons are effectively screened. The former is one of the most fundamental quantity in LQCD and has been calculated in many studies. The latter has been studied extensively, since it is calculable with LQCD more easily than the pole mass; for example, see Refs. [58, 59].

In order to understand the QGP precisely, we focus on the static-quark free energy. The static-quark free energy characterizes the quark-quark interaction in the QGP, and its color-Debye screening mass is induced by collective excitations of gluons. In phenomenological models, these play an important role in the behavior of heavy-quark bound states such as J/Ψ and Υ in the QGP that is considered to be created at the center of heavy-ion collisions [60]. In the lattice study, the static-quark free energies in the QGP can be determined from the Polyakov loop correlation functions.

The static-quark free energies have been studied so far at finite T and $\mu = 0$ in quenched QCD [21, 22, 23] and in full QCD with staggered-type quark actions [24] and Wilson-type quark actions [26, 25, 27]. The static-quark free energies at finite μ have been studied with staggered-type quark actions [28] and Wilson-type quark actions [29] by using the Taylor expansion method for the reweighting factor. We now take the imaginary-μ approach in order to obtain the static-quark free energies at real μ.

3.2 Formulation

The static-quark free energy can be defined with the Polyakov-loop operator shown in Eq. (1.6). In the lattice formulation, it is represented by

$$L(\boldsymbol{x}) = \prod_{t=1}^{N_t} U_4(\boldsymbol{x}, t) \tag{3.1}$$

with the link variables $U_\mu \in SU(3)$. After the ensemble average, the modulus and phase are defined by $\langle \mathrm{Tr} L(0) \rangle \equiv \Phi e^{i\phi}$. At imaginary μ, Φ and ϕ are order parameters of the confinement/deconfinement phase transition and the RW phase transition, respectively. With an proper gauge fixing, the static-quark free energies V_M in the color channels M can be derived from the Polyakov-loop correlators [61, 62] as

$$e^{-V_1(r,T,\mu)/T} = \frac{1}{3}\langle \mathrm{Tr} L^\dagger(\boldsymbol{x}) L(\boldsymbol{y}) \rangle, \tag{3.2}$$

$$e^{-V_8(r,T,\mu)/T} = \frac{1}{8}\langle \mathrm{Tr} L^\dagger(\boldsymbol{x}) \mathrm{Tr} L(\boldsymbol{y}) \rangle - \frac{1}{24}\langle \mathrm{Tr} L^\dagger(\boldsymbol{x}) L(\boldsymbol{y}) \rangle, \tag{3.3}$$

$$e^{-V_6(r,T,\mu)/T} = \frac{1}{12}\langle \mathrm{Tr} L(\boldsymbol{x}) \mathrm{Tr} L(\boldsymbol{y}) \rangle + \frac{1}{12}\langle \mathrm{Tr} L(\boldsymbol{x}) L(\boldsymbol{y}) \rangle, \tag{3.4}$$

$$e^{-V_{3^*}(r,T,\mu)/T} = \frac{1}{6}\langle \mathrm{Tr} L(\boldsymbol{x}) \mathrm{Tr} L(\boldsymbol{y}) \rangle - \frac{1}{6}\langle \mathrm{Tr} L(\boldsymbol{x}) L(\boldsymbol{y}) \rangle, \tag{3.5}$$

where $r = |\boldsymbol{x} - \boldsymbol{y}|$ is either the distance between a quark and an anti-quark or between two quarks, and the subscripts $M = (1, 8, 3^*, 6)$ mean the color-singlet, -octet, -antitriplet, and -sextet channels, respectively. In order to calculate the static-quark free energy in the color channels, we adopt both the Coulomb gauge fixing and the Landau gauge fixing. As shown later in Fig. 3.3, however, the latter breaks the RW periodicity of V_1 while the former preserves it. Thus we mainly use the Coulomb gauge in this study.

In this study, we consider two cases of $\mu = \mu_\mathrm{R}$ and $\mu = i\mu_\mathrm{I} = i\theta T$, where μ_R, μ_I and θ are real numbers. When $\mu = i\mu_\mathrm{I} = i\theta T$, the V_M ($M = 1, 8, 3^*, 6$) are complex. In addition, the real part of V_M is $\mathcal{C}$-even, while the imaginary part is $\mathcal{C}$-odd. This is clearly understood by expanding V_M with respect to $i\theta$:

$$\frac{V_M(r,T,\mu_\mathrm{I})}{T} = v_0(r) + iv_1(r)\theta + v_2(r)\theta^2 + iv_3(r)\theta^3 + v_4(r)\theta^4, \tag{3.6}$$

where V_M has been expanded up to the fourth order of $i\theta$. The second and the fourth term on the right-hand side of Eq. (3.6) correspond to the imaginary part of V_M. In order to obtain the static-quark free energy at real μ by analytic continuation, we replace $i\theta$ by μ_R/T:

$$\frac{V_M(r,T,\mu_\mathrm{R})}{T} = v_0(r) + v_1(r)\left(\frac{\mu_\mathrm{R}}{T}\right) - v_2(r)\left(\frac{\mu_\mathrm{R}}{T}\right)^2 - v_3(r)\left(\frac{\mu_\mathrm{R}}{T}\right)^3 + v_4(r)\left(\frac{\mu_\mathrm{R}}{T}\right)^4. \tag{3.7}$$

Note that the signs in front of the coefficients v_2 and v_3 change from plus to minus.

The WHOT-QCD Collaboration calculated the coefficients up to the second order of $\mu_{\rm R}/T$ in all the color channels by adopting a hybrid method of the Taylor expansion and the reweighting techniques with a Gaussian approximation for the distribution of the complex phase of the quark determinant [29]. Meanwhile, we calculate the coefficients up to the fourth order. Effects of the fourth-order term are not negligible as shown later.

3.3 Lattice setup

The hybrid Monte Carlo algorithm were used to generate full QCD configurations with two-flavor dynamical quarks. The simulations are performed on $N_s^3 \times N_t = 12^3 \times 4$ and the $16^3 \times 4$ lattices. As for molecular dynamics in the hybrid Monte Carlo algorithm, we take 0.01 as the step size and 100 as the step number. The acceptance ratio is about more than 95%. For all the parameter set, we generate about 16,000 trajectories and remove the first 1,000 trajectories as thermalization. We measure the heavy-quark free energy at every 100 trajectories. The relation of the parameters κ and β to the corresponding $T/T_{\rm c}$ was determined along the line of constant physics at $m_{\rm PS}/m_{\rm V} = 0.80$ [56, 57, 26], where $m_{\rm PS}$ and $m_{\rm V}$ are peudoscalor- and vector-meson masses, respectively. We show this relation in Table 4.1, together with our calculation range of θ. In this parameter setting, the pseudocritical temperature $T_{\rm c}$ is about 171 MeV and the lattice spacing a is about $0.14 \sim 0.2$ fm.

N_s	κ	β	$T/T_{\rm c}$	θ
12	0.140070	1.85	0.99(5)	$0 \sim \pi/3$
	0.138817	1.90	1.08(5)	$0 \sim \pi/3$
	0.137716	1.95	1.20(6)	$0 \sim 1.10$
	0.136931	2.00	1.35(7)	$0 \sim 1.10$
16	0.137716	1.95	1.20(6)	$0 \sim 1.20$
	0.136931	2.00	1.35(7)	$0 \sim 1.20$

Table 3.1: Summary of simulation parameter sets determined in Refs. [56, 57, 26].

3.4 Numerical results

3.4.1 Polyakov loop

First, we consider the Polyakov loop, $\langle \mathrm{Tr} L(0) \rangle \equiv \Phi e^{i\phi}$, at imaginary μ. Figures 3.1 and 3.2 show θ dependence of Φ and ϕ, respectively, and panels (a) and (b) correspond to the results of $12^3 \times 4$ and $16^3 \times 4$ lattices, respectively. For both the lattices, Φ has a cusp and ϕ has a jump from zero to $-2\pi/3$ at $\theta = \pi/3$, when $T = 1.20T_{\rm c}$ and $1.35T_{\rm c}$. The properties come from the RW transition. Note that Φ as a $\mathcal{C}$-even quantity has a mirror symmetry with respect to the line of $\theta = \pi/3$. Since ϕ as a $\mathcal{C}$-odd quantity is an order parameter of the RW transition, we can find that the critical endpoint $T_{\rm RW}$ of RW transition is located somewhere in a range of $1.08T_{\rm c} < T < 1.20T_{\rm c}$.

For $T = 1.08T_{\rm c}$, Φ rapidly decreases as θ increases, indicating that the system is in the deconfinement phase at small θ but in the confinement phase near $\theta = \pi/3$. Moreover ϕ rapidly and smoothly decreases at $\theta \gtrsim 0.7$. This means that the transition from the deconfinement phase to the confinement one is crossover. At $T = 0.99T_{\rm c}$, the system is always in the confinement phase. At $T = 1.20T_{\rm c}$ and $1.35T_{\rm c}$, on the other hand, the system is always in the deconfinement phase, and numerical results agree with each other between $12^3 \times 4$ and $16^3 \times 4$ lattices. This means that the $12^3 \times 4$ lattice is large enough. We then calculate the static-quark free energy at $T = 1.20T_{\rm c}$ and $1.35T_{\rm c}$ on the $16^3 \times 4$ lattice.

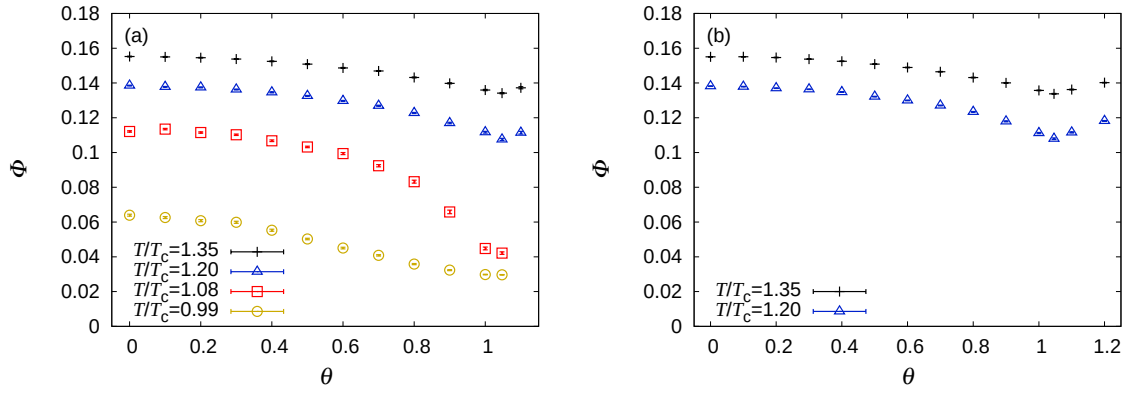

Figure 3.1: θ dependence of Φ at various values of T for (a) a $12^3 \times 4$ lattice and (b) a $16^3 \times 4$ lattice.

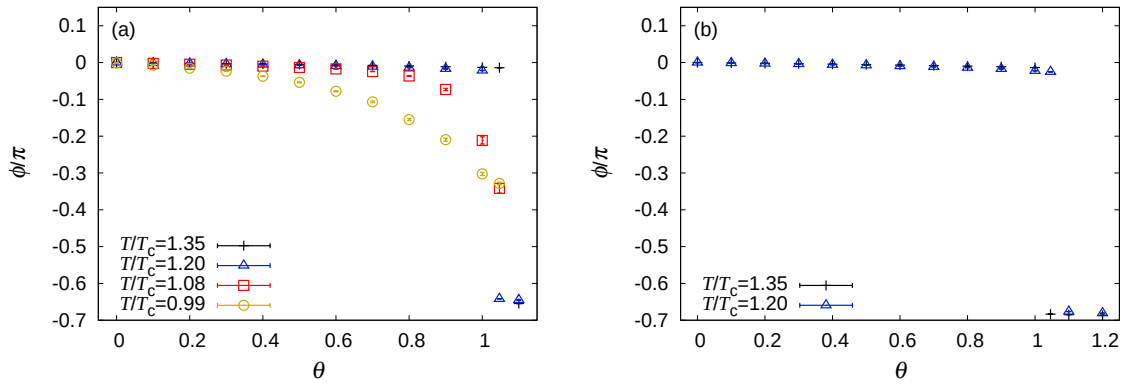

Figure 3.2: θ dependence of ϕ at various values of T for (a) a $12^3 \times 4$ lattice and (b) a $16^3 \times 4$ lattice.

3.4.2 Static-quark free energies in the color-singlet and -octet $q\bar{q}$ channels

As mentioned in Sec. 3.2, in general, the static-quark free energy is complex at imaginary μ. In fact, in the color-singlet and -octet channels ($M = 1, 8$), the V_M are $\mathcal{C}$-even and hence real, but, in the color-antitriplet and -sextet channels ($M = 3^*, 6$), they are not $\mathcal{C}$-even and then becomes complex. We consider only the real part of V_M for all the channels.

Figure 3.3 shows θ dependence of the static-quark free energy $V_1(r)/T$ in the color-singlet $q\bar{q}$ channel at $T/T_c = 1.20$ based on (a) the Coulomb and (b) the Landau gauge fixing as a function of the distance r/a between a static-quark and a static-anti-quark. Here θ varies from zero to 1.2. As mentioned in Sec. 3.4.1, $\mathcal{C}$-even quantities such as V_1 are mirror symmetric with respect to the line of $\theta = \pi/3$. This property is satisfied for the Coulomb gauge condition, but not for the Landau gauge condition. In fact, the results of $\theta = 0.9$ (1.0) do not agree with those of $\theta = 1.2$ (1.1) in the Landau gauge. This result is natural, because the Coulomb gauge condition is invariant under the $\mathbb{Z}_3$ transformation but the Landau gauge condition is not. Therefore we consider the Coulomb gauge fixing only hereafter.

Now we investigate how the fourth order coefficient $v_4(r)$ contributes to $V_1(r)$. Figure 3.4 shows the coefficients $v_2(r)$ and $v_4(r)$ for $V_1(r)$ at (a) $T = 1.20T_c$ and (b) $T = 1.35T_c$. In panel (b), the previous results [29] of the Taylor expansion method for the reweighting factor are also plotted with triangle symbols. At $T = 1.35T_c$, the

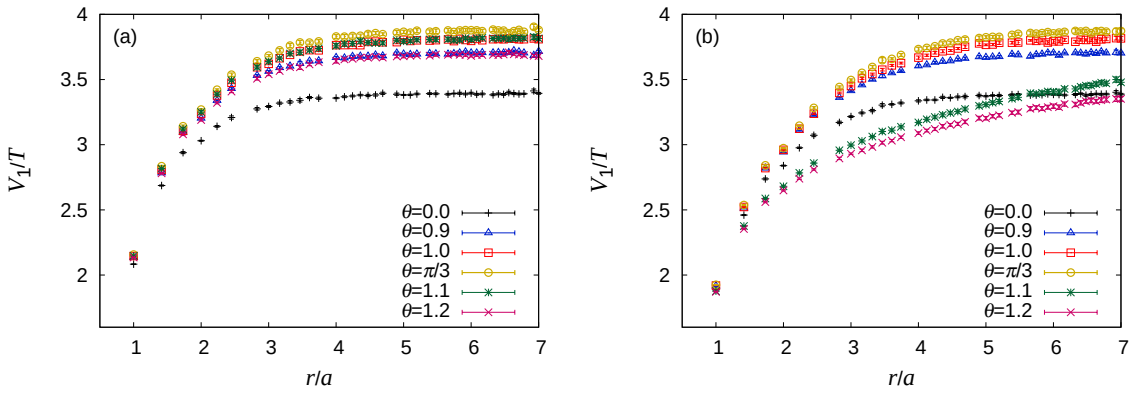

Figure 3.3: θ dependence of static-quark free energy in the color-singlet $q\bar{q}$ channel at $T/T_c = 1.20$ based on (a) the Coulomb and (b) the Landau gauge fixing as a function of the distance r/a between a static-quark and a static-anti-quark.

present results are consistent with the previous ones even though the fourth-order coefficient $v_4(r)$ are not calculated in the previous work. The ratio $v_4(r)/v_2(r)$ is about 1/4 at $T = 1.35T_c$ and 3/4 at $T = 1.20T_c$. The contribution of $v_4(r)$ to $V_1(r)$ thus becomes significant as T approaches T_c. The accuracy of the expansion form (3.6) can be investigated by comparing the original value of $V_1(r)$ and the value of the expansion form. The relative error between the two values is less than 0.5%. This indicates that the expansion is highly accurate.

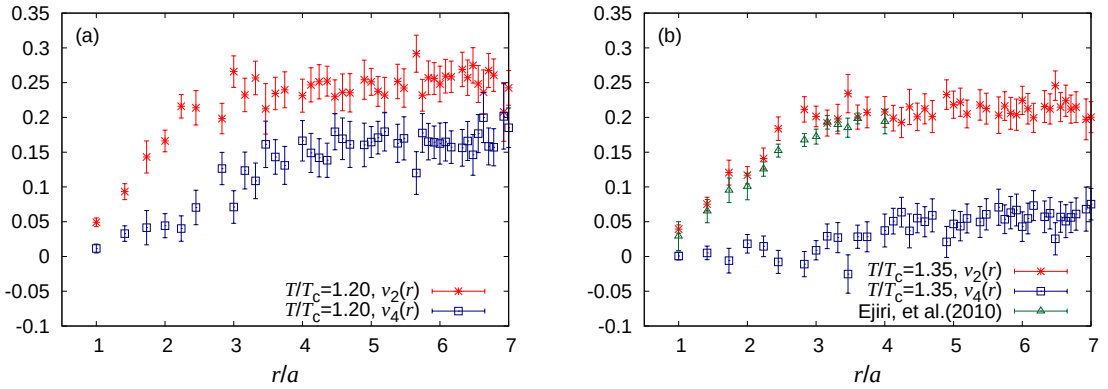

Figure 3.4: Taylor-expansion coefficients, $v_2(r)$ and $v_4(r)$, of $V_1(r)$ as a function of r/a for (a) $T = 1.20T_c$ and (b) $T = 1.35T_c$.

Figure 3.5 shows V_1/T as a function of r/a at imaginary and real μ for (a) $T/T_c =$

1.20 and (b) $T/T_c = 1.35$. Here the chemical potential varies from $(\mu/T)^2 = -1.0$ to 1.0. The color-singlet free energy V_1 is $\mathcal{C}$-even, so that $v_1(r) = v_3(r) = 0$. Furthermore, V_1 will be a linear function of $(\mu/T)^2$ if $v_4(r) = 0$. For $T/T_c = 1.20$, however, the ratio $v_4(r)/v_2(r)$ is about 0.75. Therefore, V_1/T has much weaker $(\mu/T)^2$ dependence at real μ than at imaginary μ, as shown in panel (a) of Fig. 3.5. As mentioned above, the ratio $v_4(r)/v_2(r)$ is smaller for $T/T_c = 1.35$. As a consequence of this property, V_1/T has weaker $(\mu/T)^2$ dependence at real μ than at imaginary μ, as shown in panel (b) of Fig. 3.5.

In this study, the lattice spacing a is common to all μ, so that the V_M between different values of μ/T can be compared without introducing any adjustment such as the renormalization for the short distance [24, 27]. The $V_1(r)$ yield almost the same value at small r for all μ/T in $-1 < (\mu/T)^2 < 1$. Similar behavior is seen also for temperature dependence [27].

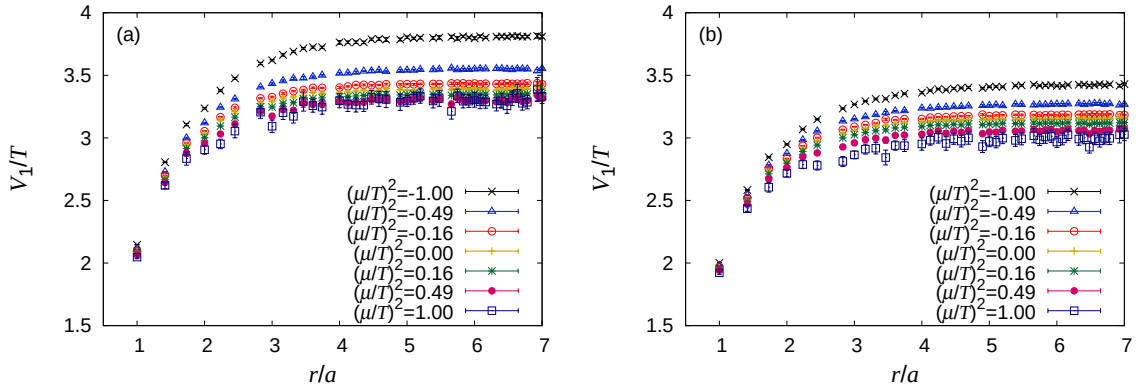

Figure 3.5: μ/T dependence of static-quark free energies in the color-singlet $q\bar{q}$ channel as a function of r/a for (a) $T/T_c = 1.20$ and (b) $T/T_c = 1.35$.

The same analysis is made for the static-quark free energies in the color-octet $q\bar{q}$ channel $V_8(r)$. Figure 3.6 shows μ/T dependence of $V_8(r)$ for (a) $T/T_c = 1.20$ and (b) $T/T_c = 1.35$. Unlike the color-singlet channel $V_1(r)$, the color-octet free energies $V_8(r)$ do not have weak μ/T dependence at small r. In fact, the magnitude decreases monotonically as $(\mu/T)^2$ increases from -1.0 to 1.0. The magnitude is weaker $(\mu/T)^2$ dependence at real μ than at imaginary μ, because $v_4(r)$ is not negligible. The V_8/T have similar r dependence among different values of μ/T. Therefore, r dependence of the force $-d(V_8/T)/d(r/a)$ is almost independent of μ/T.

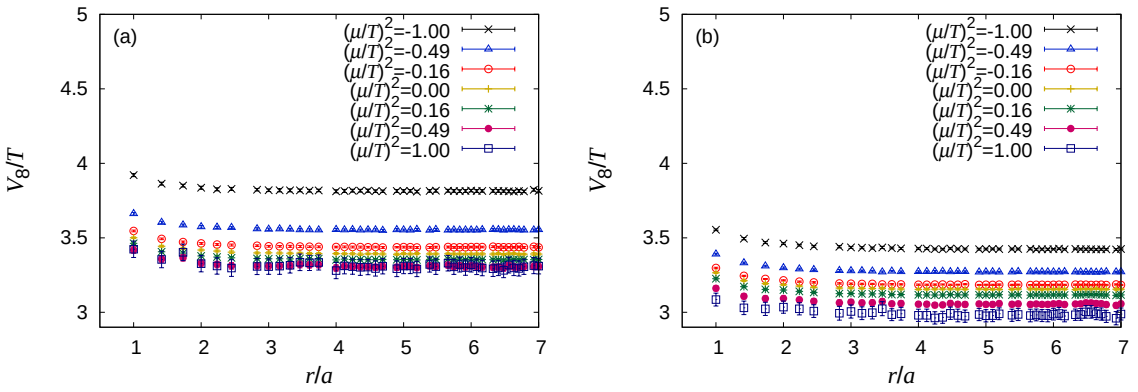

Figure 3.6: μ/T dependence of static-quark free energies in the color-octet $q\bar{q}$ channel as a function of r/a for (a) $T/T_c = 1.20$ and (b) $T/T_c = 1.35$.

For the case of $T > T_c$ and $\mu = 0$, the static-quark free energies $V_M(r)$ are known to tend to twice the single-quark free energy $2F_q(T)$ in the limit of large r [27]. This behavior persists even for finite μ. The force between static quarks is thus color screened also for finite μ. Following the previous works [26, 29, 27, 22, 23], we then subtract $2F_q(T, \theta)$ from $V_M(r)$. This subtracted static-quark free energies are convenient to see θ dependence of the force $-d(V_M/T)/d(r/a)$. The subtracted static-quark free energies are shown in Fig. 3.7 for the color-singlet and -octet channels. The color-singlet channel interaction is attractive and depends on θ, while the color-octet channel interaction is repulsive and is almost independent of θ.

3.4.3 Static-quark free energies in the color-antitriplet and -sextet qq channels

Now we consider the static-quark free energies in the color-antitriplet and -sextet qq channel V_M ($M = 3^*, 6$) , i.e., the interaction between two static quarks. Unlike V_1 and V_8, the static-quark free energies V_{3^*} and V_6 are not $\mathcal{C}$-even, so that neither the first-order coefficient $v_1(r)$ nor the third-order one $v_3(r)$ vanishes. The coefficients $v_1(r)$ and $v_3(r)$ contribute to the real part of the V_M at real μ, but not at imaginary μ, as shown in Eq. (3.7). Moreover, the coefficients were calculated up to the second order of μ/T in the previous study [29] based on the Taylor expansion method for the reweighting factor, but it is nontrivial whether the coefficients higher than the second

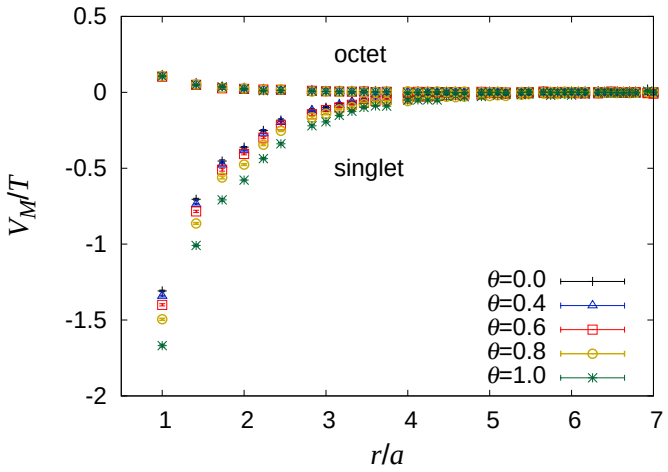

Figure 3.7: θ dependence of subtracted static-quark free energies in the color-singlet and -octet channels at $T/T_c = 1.20$.

order are negligible.

In order to investigate roles of the higher-order coefficients, we estimate $v_1(r)$, $v_2(r)$, $v_3(r)$, and $v_4(r)$ for $V_{3^*}(r)$. Figure 3.8 shows $v_1(r)$ and $v_3(r)$ as a function of the distance r/a between two static quarks, while Fig. 3.9 corresponds to $v_2(r)$ and $v_4(r)$. Here panels (a) and (b) are the results of $T = 1.20T_c$ and $T = 1.35T_c$, respectively. In panels (b) of Figs. 3.8 and 3.9, the previous results [29] are plotted by triangles. Our results are consistent with the previous results for both $v_1(r)$ and $v_2(r)$, although $v_3(r)$ and $v_4(r)$ were not calculated in the previous work of Ref. [29]. The ratio $v_3(r)/v_1(r)$ is about 0.71 at $T = 1.20T_c$ and about 0.33 at $T = 1.35T_c$. This indicates that the contribution of $v_3(r)$ to V_{3^*} is not negligible. Similar discussion is possible for $v_4(r)$. The ratio $v_4(r)/v_2(r)$ in V_{3^*} is about 0.7 at $T = 1.20T_c$ and about 0.25 at $T = 1.35T_c$. These ratios are comparable to those in V_1. Thus the coefficient $v_4(r)$ is also not negligible in the case of V_{3^*}. Again, the accuracy of the expansion form (3.6) is investigated by the relative error between the original value of $V_{3^*}(r)$ and the value of the expansion form. The error is less than 0.5%, indicating that the expansion is accurate.

Figures 3.10 and 3.11 show the real part of static-quark free energies in the color-antitriplet and -sextet qq channels as a function of r/a, respectively, for (a) $T/T_c = 1.20$ and (b) $T/T_c = 1.35$. Unlike the color-singlet channel $V_1(r)$, the values of V_{3^*}/T

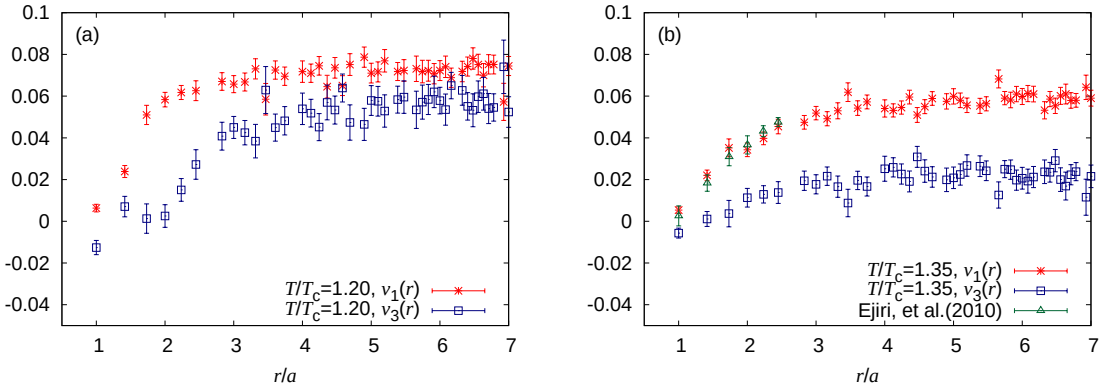

Figure 3.8: Taylor-expansion coefficients, $v_1(r)$ and $v_3(r)$, of $V_{3^*}(r)$ as a function of distance r/a between two static quarks for (a) $T = 1.20T_c$ and (b) $T = 1.35T_c$.

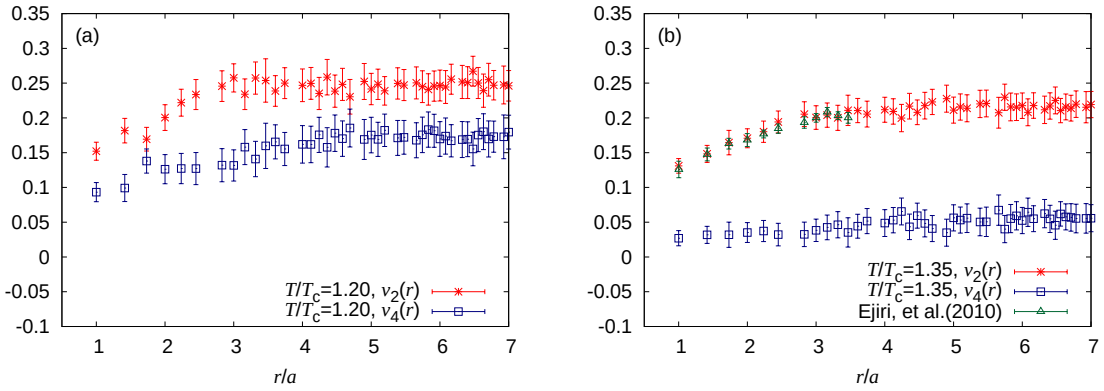

Figure 3.9: Taylor-expansion coefficients, $v_2(r)$ and $v_4(r)$, of $V_{3^*}(r)$ as a function of r/a for (a) $T = 1.20T_c$ and (b) $T = 1.35T_c$.

and V_6/T depend on μ/T even at small r. Meanwhile, the magnitude decreases monotonically as $(\mu/T)^2$ increases from -1.0 to 1.0. The static-quark free energies V_{3^*} and V_6 have weaker $(\mu/T)^2$ dependence at real μ than at imaginary μ, because $v_1(r)$, $v_3(r)$, and $v_4(r)$ are non-negligible compared with $v_2(r)$.

Again, the static-quark free energies tend to twice the single-quark free energy at large distance, indicating that the color screening takes place also in these non-singlet channels even for finite μ. Now twice the single-quark free energy is subtracted from V_{3^*} and V_6. The results are shown in Fig. 3.12. The antitriplet channel interaction is attractive and has weak θ dependence, while the sextet channel interaction is repulsive and hardly depends on θ.

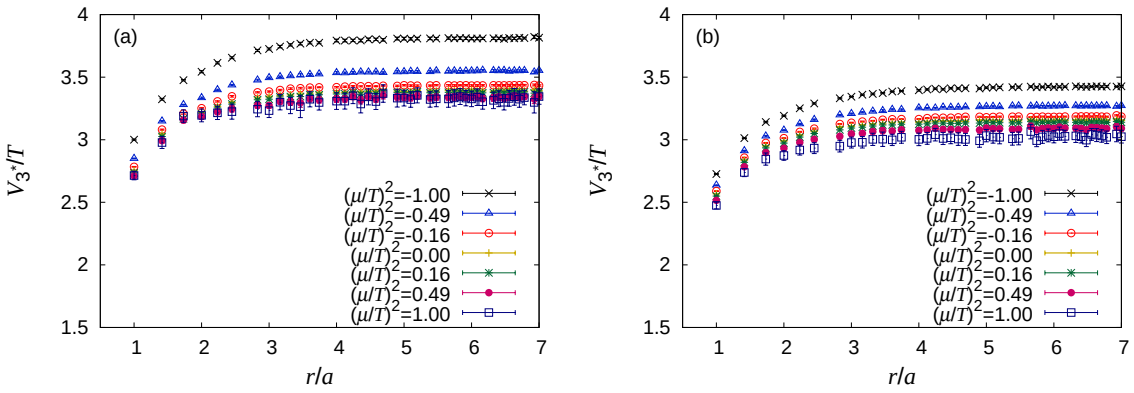

Figure 3.10: μ/T dependence of the real part of static-quark free energies in the color-antitriplet qq channel as a function of r/a for (a) $T/T_c = 1.20$ and (b) $T/T_c = 1.35$.

3.5 Color Debye screening

In this section, we consider the color-Debye screening. Our results on the static-quark free energies show that the color screening takes place at both imaginary and real μ. It is likely that the color-screening effect is caused by the effective mass of gluon. Originally, the gluon is massless, but gains an effective mass at finite T and μ due to the collective excitation. This effective mass shortens the distance of interactions between quarks. Namely, the interactions are masked at finite T and μ. This is nothing but the color screening, and the effective mass is called color-Debye screening

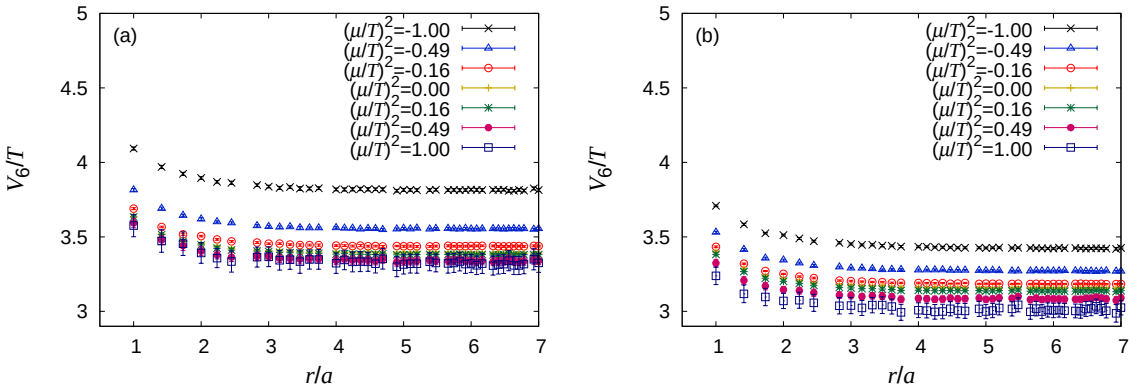

Figure 3.11: μ/T dependence of the real part of static-quark free energies in the color-sextet qq channel as a function of r/a for (a) $T/T_c = 1.20$ and (b) $T/T_c = 1.35$.

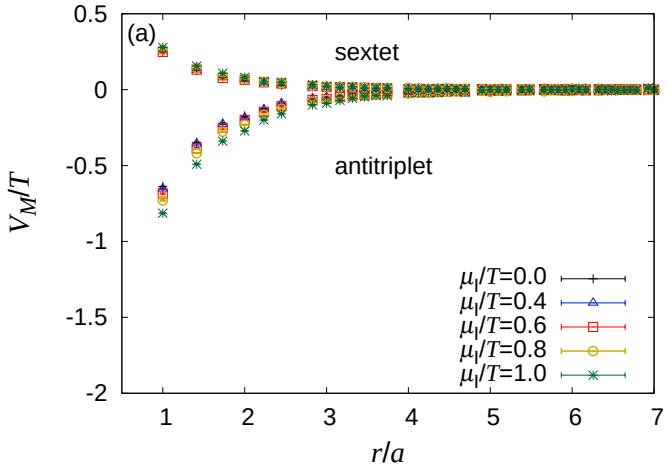

Figure 3.12: θ dependence of subtracted static-quark free energies in the color-antitriplet and -sextet channels at $T/T_c = 1.20$.

mass.

In order to study the color screening, we fit the static-quark free energies by the screened Coulomb form

$$V_M(r,T,\mu) = C_M \frac{\alpha_{\rm eff}(T,\mu)}{r} e^{-m_D(T,\mu)r}, \tag{3.8}$$

where $\alpha_{\rm eff}$ and $m_D(T,\mu)$ are the effective running coupling and the Debye screening mass, respectively. The Casimir factor $C_M \equiv \langle \sum_{a=1}^{8} t_1^a \cdot t_2^a \rangle_M$ for color channel M is obtained as

$$C_1 = -\frac{4}{3},\ C_8 = \frac{1}{6},\ C_6 = \frac{1}{3},\ C_{3^*} = -\frac{2}{3}. \tag{3.9}$$

First we focus our attention on the color-singlet channel since it is the physical channel. The subtracted static-quark free energy should be used to extract the color-Debye screening mass, because $V_M = 0$ in the limit of large r in Eq. (3.8). Following the previous study [26], we choose the fitting range of $\sqrt{11} \le r/a \le 6.0$.

The color-Debye screening mass can be calculated with hard-thermal-loop perturbation theory (HTLpt). In the leading order (LO) and the massless-quark limit, the color-Debye screening mass is given by

$$\frac{m_D(T,\mu)}{T} = g_{\rm 2l}(\nu)\sqrt{\left(1+\frac{N_f}{6}\right) + \frac{N_f}{2\pi^2}\left(\frac{\mu}{T}\right)^2}, \tag{3.10}$$

where $g_{\rm 2l}$ is the 2-loop running coupling given by

$$g_{\rm 2l}^{-2}(\nu) = \beta_0 \ln\left(\frac{\nu}{\Lambda}\right)^2 + \frac{\beta_1}{\beta_0}\ln\ln\left(\frac{\nu}{\Lambda}\right)^2, \tag{3.11}$$

where the argument in the logarithms can be written as $\nu/\Lambda = (\nu/T)(T/T_{\rm c})(T_{\rm c}/\Lambda)$, with $\Lambda = \Lambda_{\overline{\rm MS}}^{N_f=2} \simeq 261$ MeV [63] and $T_{\rm c} \simeq 171$ MeV [56], and the renormalization point ν is assumed to be $\nu = \sqrt{(\pi T)^2 + \mu^2}$ [64]. Beyond the LO calculation, the color-Debye screening mass was estimated in the next-to-next-to-leading order (NNLO) [65] with the Braaten-Nieto prescription [66] that is an effective field theory based on "dimensional reduction."

Figure 3.13 shows the color-Debye screening mass in the color-singlet channel as a function of $(\mu/T)^2$ at $T = 1.20T_{\rm c}$. The crosses and the filled circle with error bar

denote the present results and the previous result [26], respectively, and the dotted and solid lines represent the results of the LO and the NNLO perturbation theory, respectively.

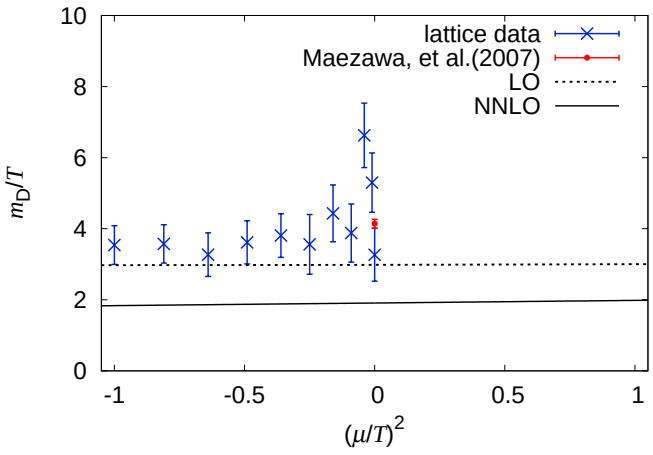

Figure 3.13: Comparison of lattice results with HTLpt results for $m_{\rm D}$ as a function of $(\mu/T)^2$ at $T/T_{\rm c} = 1.20$.

Figure 3.14 shows $(\mu/T)^2$ dependence of m_D/T for (a) $T = 1.20T_{\rm c}$ and (b) $1.35T_{\rm c}$. In order to estimate m_D at real μ, we expand m_D up to the second order of μ/T,

$$\frac{m_D}{T} = a_0(T) + a_2(T)\left(\frac{\mu}{T}\right)^2. \tag{3.12}$$

Note that m_D is $\mathcal{C}$-even, so that it has no linear term of μ/T. The coefficients $a_0(T)$ and $a_2(T)$ are determined from m_D at imaginary μ with a χ^2 fitting:

$$\frac{m_D}{T} = (4.41 \pm 0.34) + (1.15 \pm 0.60)\left(\frac{\mu}{T}\right)^2 \tag{3.13}$$

for $T = 1.20T_{\rm c}$ and

$$\frac{m_D}{T} = (3.93 \pm 0.25) + (0.58 \pm 0.44)\left(\frac{\mu}{T}\right)^2 \tag{3.14}$$

for $T = 1.35T_{\rm c}$. The plus sign in front of the coefficient $a_2(T)$ is changed into the minus one in m_D at real μ. The resulting m_D/T is shown by a hatched area in Fig. 3.14. For both $T = 1.20T_{\rm c}$ and $1.35T_{\rm c}$, our results are consistent with the previous LQCD

results [26]. Figure 3.14 also shows the results of the NNLO HTLpt calculations at $\nu = \pi\sqrt{T^2 + \mu^2/\pi^2}$ (dashed line) and at $\nu = 4\pi\sqrt{T^2 + \mu^2/\pi^2}$ (solid line), respectively. Our results are bigger than the LO and NNLO predictions in magnitude. Moreover our results have stronger $(\mu/T)^2$ dependence than the LO and NNLO predictions.

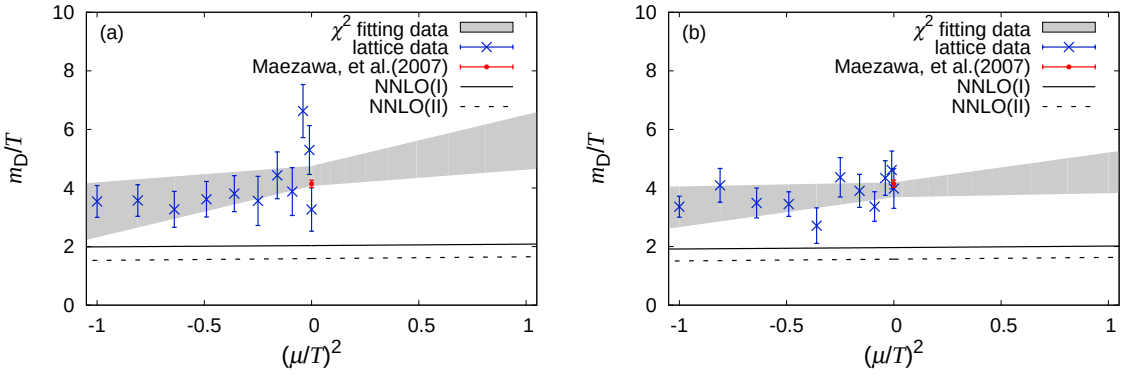

Figure 3.14: $(\mu/T)^2$ dependence of color-Debye screening mass in the color-singlet channel for (a) $T/T_c = 1.20$ and (b) 1.35.

In principle, the same analysis can be made for the subtracted static-quark free energies in the nonsinglet channel. However it is difficult to extract m_D from the free energies in the octet and sextet channels, because the free energies have small μ/T dependence and the magnitudes are also small. We then consider only the antitriplet channel. Figure 3.15 shows $(\mu/T)^2$ dependence of the color-Debye screening mass in the color-antitriplet channel for (a) $T = 1.20T_c$ and (b) $1.35T_c$. Again, in order to obtain m_D at real μ, we determined the coefficients $a_0(T)$ and $a_2(T)$ from LQCD data at imaginary μ with a χ^2 fitting:

$$\frac{m_D}{T} = (3.90 \pm 0.35) + (0.79 \pm 0.72)\left(\frac{\mu}{T}\right)^2 \tag{3.15}$$

for $T = 1.20T_c$ and

$$\frac{m_D}{T} = (4.12 \pm 0.28) + (0.58 \pm 0.51)\left(\frac{\mu}{T}\right)^2 \tag{3.16}$$

for $T = 1.35T_c$. The resulting m_D/T is shown by the hatched areas in Fig. 3.15. For both $T = 1.20T_c$ and $1.35T_c$, our results are consistent with the previous LQCD results [26]. The m_D in the antitriplet channel are similar to those in the singlet one

in both magnitude and $(\mu/T)^2$ dependence. Thus, our results are bigger than the perturbation predictions in magnitude and stronger in $(\mu/T)^2$ dependence.

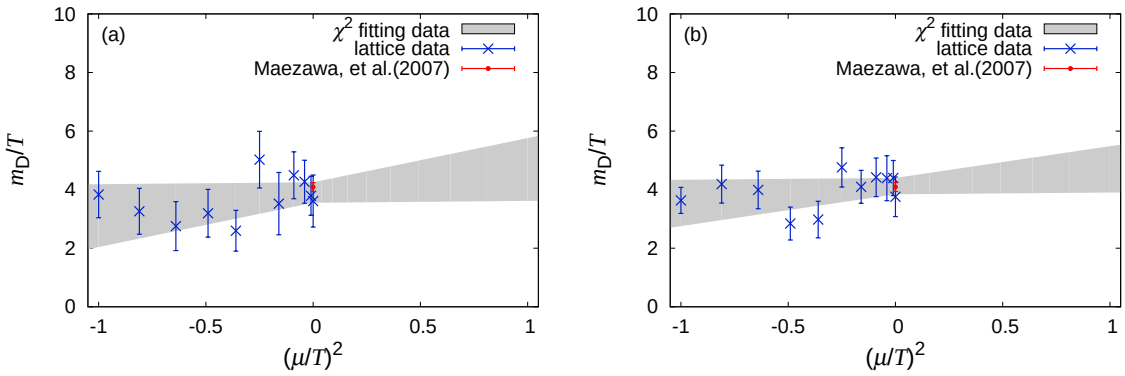

Figure 3.15: $(\mu/T)^2$ dependence of color-Debye screening mass in the color-antitriplet channel for (a) $T/T_c = 1.20$ and (b) 1.35.

3.6 Short summary

We have researched μ dependence of the static-quark free energies at both imaginary and real μ. LQCD simulations were performed on a $16^3 \times 4$ lattice with the two-flavor clover-improved Wilson quark action and the renormalization-group-improved Iwasaki gauge action at imaginary μ. We considered two cases of $T = 1.20T_c$ and $1.35T_c$ and took an intermediate quark mass corresponding to the line of constant physics at $m_{PS}/m_V = 0.80$. The static-quark free energies at imaginary μ were expanded up to the fourth order of $\theta(= \mu_I/T)$, and then extrapolated to real μ by replacing $i\theta$ with μ_R/T.

Calculating static-quark free energies in the color-singlet cannel, we found that the RW periodicity is kept in the Coulomb gauge fixing but not in the Landau gauge one. Since the Taylor expansion coefficients were calculated up to the second order in the previous study [29], we studied the forth-order contribution with the Wilson-type quark action. We found that the fourth-order term weakens $(\mu/T)^2$ dependence of the static-quark free energy for the color-singlet channel at real μ. This indicates that the contribution is not negligible. Moreover this contribution becomes more significant as T approaches T_c. These results are true also for the nonsinglet channels.

At large distances, the static-quark free energies tend to twice the single-quark free energy in all the color channels. This property was already known for finite T and zero μ [27], but the present analysis show that the property persists also for finite μ. For both imaginary and real μ, the static-quark free energies are attractive in the color-singlet and -antitriplet channels, whereas they are repulsive in the color-octet and -sextet channels. The attractive interactions have stronger μ/T dependence than the repulsive ones.

Finally, in order to analyze the screening effect of color charges at finite μ, we have investigated μ dependence of the color-Debye screening mass in both the imaginary and the real μ region. The color-Debye screening mass was extracted from LQCD data on the static-quark free energies at imaginary μ by assuming the screened Coulomb form, and was extrapolated to real μ by expanding it with respect to $\mu_{\rm I}/T$ up to the second order and replacing $i\theta$ by $\mu_{\rm R}/T$. As for m_D/T, our results are bigger than the predictions of HTLpt in magnitude and stronger in $(\mu/T)^2$ dependence.

Chapter 4

Quark number density

In this chapter, we study properties of the quark number density n_q by using LQCD and the hadron resonance gas (HRG) model. The quark number density is calculated at imaginary μ with LQCD simulations on an $8^2 \times 16 \times 4$ lattice with the clover-improved $N_f = 2$ Wilson fermion action and the renormalization-group-improved Iwasaki gauge action. The results at imaginary μ are consistent with the previous results of the staggered-type quark action. The n_q obtained at imaginary μ are extrapolated to real μ by assuming a Fourier series for the confinement region and a polynomial series for the deconfinement region. The extrapolated results are consistent with the previous results of the Taylor expansion method for the reweighting factor. The upper bound $(\mu/T)_{\rm max}$ of the reliable extrapolated region is estimated for each T. We examine whether T dependence of nucleon and Δ-resonance masses can be estimated from the LQCD results on n_q at imaginary μ by using the HRG model. In our test calculation, nucleon and Δ-resonance masses reduce by about 10% near $T_{\rm c}$.

4.1 Introduction

In general, particle number density becomes nonzero when the corresponding chemical potential is finite. In QCD, the quark number density n_q is an essential quantity to study high-density physics at finite μ. In fact, n_q is often calculated to study the QCD phase diagram and the equation of state (EOS) at finite μ. In particular, the EOS is important to understand the mechanism of supernovae and the inner structure of neutron stars (NSs).

Recently, two-solar-mass ($2M_\odot$) neutron stars (NSs) were observed [67]. This indicates that the EOS is comparatively stiff. In NJL-type effective models, n_q and the

stiffness of the EOS are quite sensitive to the strength G_v of vector-type interaction. In the entanglement-PNJL (EPNJL) model, $G_v = 0.03G_s$ is the lower bound of G_v to reproduce the $2M_\odot$ observation [68], where G_s is the strength of scalar-coupling interaction. For the lower bound of G_v, the critical baryon chemical potential $\mu_{\rm cB}$ of hadron-quark phase transition becomes $\mu_{\rm cB} \sim 1.6$ GeV at $T = 0$. This value is the lower bound of $\mu_{\rm cB}$ to account for the observations of $2M_\odot$ NSs, since $\mu_{\rm cB}$ increases as G_v becomes large. In Ref. [69], the vector coupling is determined to be $G_v = 0.33G_s$ from LQCD data on n_q [29].

At imaginary μ where the LQCD simulation is available, n_q as well as the phase of the Polyakov loop is the order parameter of the RW transition, because these are $\mathcal{C}$-odd quantities [74]. In Ref. [71], the properties of n_q were investigated with the PNJL model that possesses the RW periodicity. The RW transition were confirmed by calculating n_q with staggered-type quark action [35, 36].

For small real μ/T, the quark number density n_q was calculated directly by using the Taylor-expansion method for the reweighting factor with the staggered-type [30] and the Wilson-type quark action [29] and by using the multi-parameter reweighting method with the Wilson-type quark action [33]. In Refs. [35, 36, 37, 39], n_q was calculated at imaginary μ only with staggered-type quark action and extrapolated to real μ with analytic continuation. We then take the Wilson-type quark action to calculate n_q at imaginary μ, and extrapolate it to real μ with analytic continuation.

The HRG model are often used to analyze LQCD data at $T \lesssim T_{\rm c}$. In the HRG model, baryons and mesons are treated as free particles. By comparing LQCD data with the HRG results, we investigate how the strong interaction affects thermodynamics. This is a guide to construct the effective model. Actually, the HRG model was combined with the chiral perturbation theory in Ref. [72]. In addition, baryon masses were deduced from LQCD data on the quark number susceptibilities with the HRG model [73]. We thus test whether one can determine T dependence of baryon masses from LQCD results on n_q at imaginary μ by using the HRG model.

4.2 Formulation

4.2.1 Quark number density

The quark number density n_q is defined as

$$\frac{n_q}{T^3} = \frac{1}{VT^2}\frac{\partial}{\partial\mu}\ln Z \tag{4.1}$$

$$= \frac{N_f N_t^3}{N_V}\mathrm{tr}\left[M^{-1}\frac{\partial M}{\partial\hat{\mu}}\right], \tag{4.2}$$

where V is the three-dimensional volume, N_f is the number of flavors, N_t is the temporal lattice size, N_V is the lattice volume and M is the fermion matrix. We apply the random noise method for the trace in Eq. (4.2). The number of noise vectors is about 4,000. The QCD partition function Z is μ-even, so that n_q is μ-odd from Eq. (4.1). This means that n_q is purely imaginary in the imaginary μ region;

$$n_q^* = \left(\frac{1}{V}\frac{\partial \ln Z}{\partial(i\theta)}\right)^* = \frac{1}{V}\frac{\partial \ln Z}{\partial(-i\theta)} = -n_q. \tag{4.3}$$

For later convenience, we define n_q^{I} as the imaginary part of n_q: $n_q^{\mathrm{I}} = \mathrm{Im}(n_q)$. We have also confirmed that the real part of n_q is zero at any T and imaginary μ in our LQCD simulations.

4.2.2 Analytic continuation

Our goal is to obtain n_q at real μ. For this purpose, we fit an analytic function to our LQCD results on n_q at imaginary μ and extrapolate the function to real μ.

In the confinement region at $T < T_{\mathrm{c}}$, the quark number density is smooth for any θ and a θ-odd periodic function because of RW periodicity. These properties have been confirmed with LQCD in Refs. [35, 36, 39] and with the effective models in Refs. [74, 75, 76]. In addition, observables obtained from the QCD partition function can be described by the fugacity $e^{i\mu_{\mathrm{I}}/T}$ at imaginary μ. Therefore, n_q can be described by a Fourier series as

$$\frac{n_q(T, i\theta)}{T^3} \approx iS_F^n(T,\theta) = i\sum_{k=1}^{n} a_F^{(k)}(T)\sin(3k\theta), \tag{4.4}$$

where the superscript n of $S_F^n(T,\theta)$ denotes the highest order in the partial sum. The coefficients $a_F^{(k)}(T)$ are obtained by fitting the function (4.4) to LQCD results at imaginary μ. When the function is extrapolated from imaginary to real μ, the factor $e^{i\mu_{\rm I}/T}$ is replaced by $e^{\mu/T}$ in Eq. (4.4):

$$\frac{n_q(T,\mu/T)}{T^3} \approx g_F^n\left(T,\frac{\mu}{T}\right) = \sum_{k=1}^{n} a_F^{(k)}(T)\sinh\left(3k\frac{\mu}{T}\right). \tag{4.5}$$

Note that the coefficients $a_F^{(k)}(T)$ have already been determined at imaginary μ.

In the region $T_{\rm c} < T < T_{\rm RW}$, θ dependence of n_q is complicated. For small θ, the system is in the deconfinement region, but it becomes in the confinement region for large θ near $\pi/3$ because of the deconfinement/confinement transition. This property makes the analytic continuation difficult. We thus do not perform the analytic continuation in this region of T.

In the deconfinement region at $T > T_{\rm RW}$, the quark number density is not smooth at $\theta(=\mu_{\rm I}/T) = \pi/3$ where the RW first-order transition occurs; note that n_q is the order parameter of the first-order transition [74]. It is expected from this property that n_q monotonically increases with θ and can be described by a polynomial series of θ for $T > T_{\rm RW}$ and $\theta < \pi/3$:

$$\frac{n_q(T,i\theta)}{T^3} \approx iS_p^{2n-1}(T,\theta) = i\sum_{k=1}^{n} a_p^{(2k-1)}(T)\theta^{2k-1}, \tag{4.6}$$

where the superscript n of $S_p^{2n-1}(T,\theta)$ denotes the highest order in the partial sum. Again, in order to extrapolate this function from imaginary μ to real μ, we replace $i\theta$ by μ/T in Eq. (4.6):

$$\frac{n_q(T,\mu/T)}{T^3} \approx g_p^{2n-1}\left(T,\frac{\mu}{T}\right) = \sum_{k=1}^{n}(-)^{(k-1)}a_p^{(2k-1)}(T)\left(\frac{\mu}{T}\right)^{2k-1}. \tag{4.7}$$

Of course, the coefficients $a_p^{(k)}(T)$ have already been determined at imaginary μ.

4.3 Lattice setup

Full QCD configurations with two-flavor dynamical quarks were generated with the Hybrid Monte Carlo algorithm. The simulations were performed on a lattice of $N_x \times N_y \times N_z \times N_t = 8^2 \times 16 \times 4$. The reason why we took the lattice is to reduce the simulation time and take more trajectories, but the n_q calculated on an $8^2 \times 16 \times 4$ lattice is confirmed to be consistent with the previous results [36, 39] on a $16^3 \times 4$ lattice. The step size of molecular dynamics is 0.02 and the step number of molecular dynamics is 50. The acceptance ratio is more than 95%. We generated about 32,000 trajectories and removed the first 4,000 trajectories as thermalization for all the parameter set. The number of trajectories is larger than in the previous studies [36, 39]. We measured n_q at every 100 trajectories. The relation of the parameters κ and β to the corresponding $T/T_{\rm c}$ was determined along the line of constant physics at $m_{\rm PS}/m_{\rm V} = 0.80$ [56, 57, 26], where $m_{\rm PS}$ and $m_{\rm V}$ are peudoscalor- and vector-meson masses, respectively. We show this relation in Table 4.1, together with our calculation range of θ. The n_q were calculated at $0 \leq \theta \leq \pi/3$ for β from 1.80 to 2.00 and $0 \leq \theta \leq 1.4$ for $\beta = 2.20$. The pseudocritical temperature $T_{\rm c}$ and the lattice spacing a are the same as in Sec. 3.3.

κ	β	$T/T_{\rm c}$	θ
0.141139	1.80	0.93(5)	$0 \sim \pi/3$
0.140070	1.85	0.99(5)	$0 \sim \pi/3$
0.138817	1.90	1.08(5)	$0 \sim \pi/3$
0.137716	1.95	1.20(6)	$0 \sim \pi/3$
0.136931	2.00	1.35(7)	$0 \sim \pi/3$
0.135010	2.20	2.07(10)	$0 \sim 1.4$

Table 4.1: Summary of simulation parameter sets determined in Refs. [56, 57, 26].

4.4 Numerical results

4.4.1 Quark number density at imaginary μ

Figure 4.1 shows θ dependence of $n_q^{\rm I}/T^3$ at $T = 2.07T_{\rm c}$. LQCD data are plotted by symbols with error bars, although the errors are quite small. The data jumps down

from about +4.3 to about −4.3 at $\theta = \pi/3$, since n_q is a $\mathcal{C}$-odd quantity. Thus, LQCD simulations with the Wilson-type fermion action also shows that the RW transition takes place.

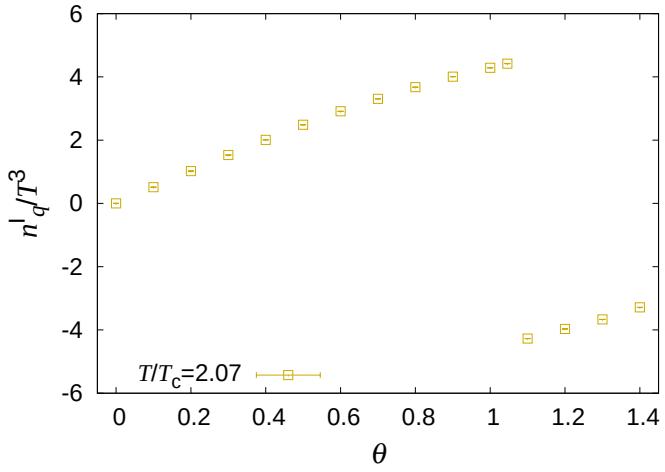

Figure 4.1: θ dependence of $n_q^{\rm I}/T^3$ at $T = 2.07T_{\rm c}$.

Figure 4.2 shows θ dependence of $n_q^{\rm I}/T^3$ for all the temperatures we consider. The LQCD data are plotted by symbols with error bars, although the errors are quite small. When the temperature is below $T_{\rm c}$, $n_q^{\rm I}/T^3$ behaves as the sine function. When the temperature is above $T_{\rm RW}$, $n_q^{\rm I}/T^3$ increases monotonically up to $\theta = \pi/3$. At $T = 1.08T_{\rm c}$, the crossover transition occurs at $\theta \simeq 0.8$. Therefore, $n_q^{\rm I}/T^3$ increases monotonically up to $\theta \sim 0.7$ but decreases to zero for $\theta > 0.8$. Our results are consistent with the results of the staggered-type fermion in Ref. [39]. Thus this indicates that n_q obtained is independent of the fermion action taken.

First we consider the case of $T < T_{\rm c}$. The coefficients $a_F^{(k)}$ in the Fourier series are determined from LQCD data on n_q at imaginary μ. In principle, the n_q is described by the infinite sum of the sine functions at imaginary μ and the hyperbolic sine functions at real μ. When the series converges, the partial sum becomes valid. For the convergence, the coefficient $a_F^{(k)}$ should decrease as the order becomes high. When this property is satisfied, we can deduce the coefficients $a_F^{(k)}$ from LQCD data.

In Fig. 4.3, the χ^2 fittings are compared with LQCD data. LQCD data are represented by green symbols, and fitting results of S_F^1 and S_F^2 are drawn with dashed and solid lines, respectively. The errors of $a_F^{(1)}$ and $a_F^{(2)}$ are within the thickness of lines.

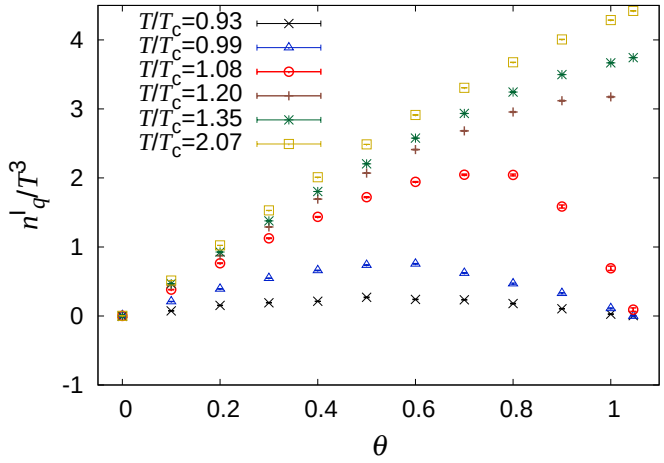

Figure 4.2: θ dependence of $n_q^{\rm I}/T^3$ at various values of T.

The fitting range is $0 \le \theta \le \pi/3$ in any case of S_F^n. Coefficients of the Fourier series are tabulated in Table 4.2 for three cases of S_F^1, S_F^2 and S_F^3 together with χ^2/dof. As for $T = 0.93T_{\rm c}$, the values of the χ^2/dof indicate that all the χ^2 fittings by S_F^1, S_F^2 and S_F^3 are almost the same quality. In S_F^3, however, the absolute value of $a_F^{(2)}$ is much smaller than that of $a_F^{(1)}$, but the absolute value of $a_F^{(3)}$ is comparable with that of $a_F^{(2)}$. This means that the values of the coefficients higher than $a_F^{(2)}$ cannot be determined from the present LQCD data. Thus the result of S_F^2 is acceptable but that of S_F^3 is not. As for $T = 0.99T_{\rm c}$, the χ^2 fitting by S_F^2 is much better than that by S_F^1, so that the result of S_F^2 is more acceptable than that of S_F^1. On the other hand, the χ^2 fitting by S_F^3 is almost the same quality as that by S_F^2. In addition, the absolute value of $a_F^{(3)}$ is comparable with that of $a_F^{(2)}$ in S_F^3, if we consider the error ranges of $a_F^{(2)}$ and $a_F^{(3)}$. Therefore, the values of the coefficients higher than a_F^2 cannot be determined from the present LQCD data, and then it is obvious that the result of S_F^2 is acceptable but that of S_F^3 is not. Thus we take S_F^1 and S_F^2 for the extrapolation of n_q from imaginary μ to real μ below $T_{\rm c}$.

Next we consider the case of $T > T_{\rm RW}$. The coefficients $a_p^{(k)}$ in the polymonial series are determined from LQCD data on n_q at imaginary μ. Figure 4.4 shows χ^2 fittings to LQCD data for S_p^3 in panel (a) and for S_p^5 in panel (b). For each panel, LQCD data are represented by symbols with error bars, and for each case of $T = 1.20T_{\rm c}$, $1.35T_{\rm c}$ and $2.07T_{\rm c}$, a pair of dashed lines stand for the upper and lower bounds of χ^2 fittings,

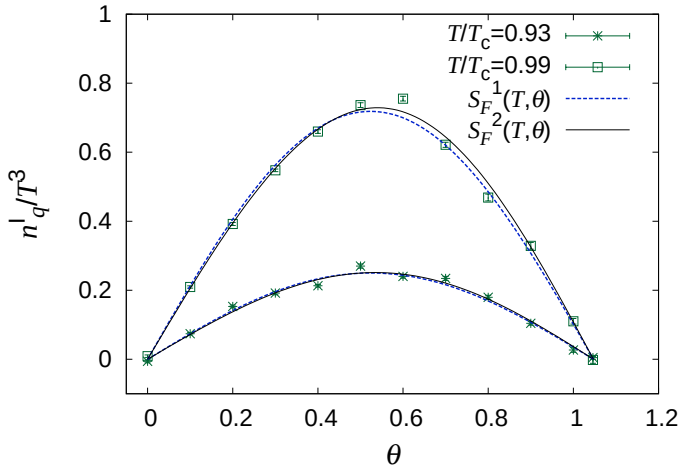

Figure 4.3: Results of χ^2 fittings to LQCD data for $T < T_c$.

T/T_c	$a_F^{(1)}$	$a_F^{(2)}$	$a_F^{(3)}$	χ^2/dof
0.93	0.250(2)			5.937
0.93	0.251(2)	−0.00457(216)		6.084
0.93	0.251(2)	−0.00526(219)	0.00440(214)	6.290
0.99	0.718(2)			11.06
0.99	0.728(3)	−0.0179(26)		7.453
0.99	0.727(3)	−0.0137(30)	−0.00825(276)	7.288

Table 4.2: Coefficients of Fourier series for S_F^1, S_F^2, and S_F^3.

respectively. The fitting range is $0 \leq \theta \leq 1$ in any case of S_p^n. The fitting results well reproduce the LQCD data. Coefficients of the polynomial series are tabulated in Table 4.3 for three cases of S_p^3, S_p^5 and S_p^7 together with χ^2/dof. As for each T, the fitting of S_p^7 has the smallest value of χ^2/dof. Especially in the case of $T = 1.35T_c$, the value of χ^2/dof is almost one. However, the absolute value of $a_p^{(7)}$ is comparable with that of $a_p^{(5)}$, while the absolute value of $a_p^{(5)}$ is much smaller than that of $a_p^{(3)}$. This indicates that the coefficient $a_p^{(7)}$ cannot be determined from the present LQCD data. Therefore, we take S_p^3 and S_p^5 for the extrapolation of n_q from imaginary μ to real μ above $T_{\rm RW}$.

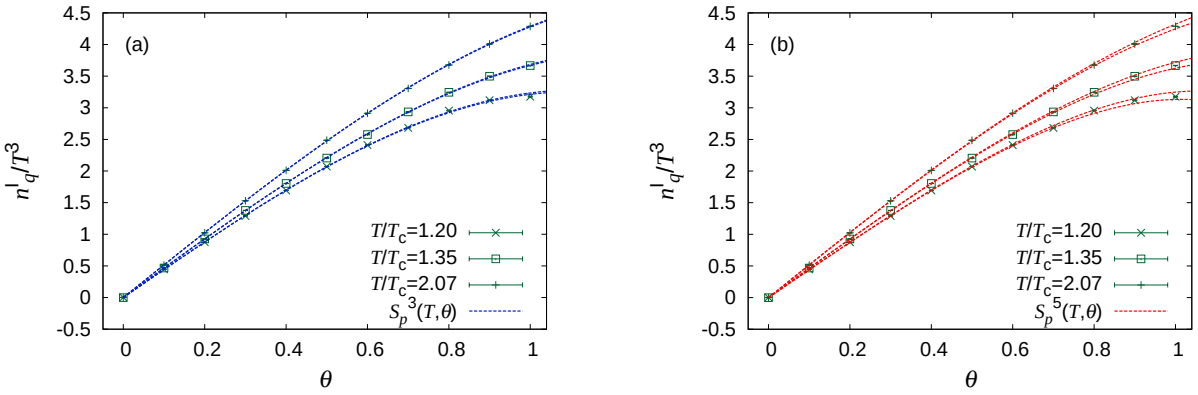

Figure 4.4: Results of χ^2 fittings to LQCD data for above $T > T_{\rm RW}$.

4.4.2 Quark number density at real μ

First we consider the case of $T < T_c$. The n_q at imaginary μ are extrapolated to real μ by using g_F^1 and g_F^2. Figure 4.5 shows μ/T dependence of n_q/T^3 at $T = 0.99T_c$. The green symbol with error bar denotes the previous lattice results obtained by using the Taylor expansion method for the reweighting factor in Ref. [29]. A pair of lines mean the upper and lower bounds of the extrapolation, and the dashed (solid) lines correspond to the results of $g_F^1(g_F^2)$. The bounds of g_F^1 stem from the error of $a_F^{(1)}$, while those of g_F^2 come from the errors of $a_F^{(1)}$ and $a_F^{(2)}$. The result of g_F^1 is consistent with the previous lattice result of the Taylor expansion method for the reweighting

T/T_c	$a_p^{(1)}$	$a_p^{(3)}$	$a_p^{(5)}$	$a_p^{(7)}$	χ^2/dof
1.20	4.437(4)	−1.214(7)			13.66
1.20	4.407(5)	−1.024(27)	−0.1935(260)		8.472
1.20	4.427(7)	−1.274(66)	0.4458(1569)	−0.4229(1024)	7.245
1.35	4.675(3)	−0.9973(49)			6.036
1.35	4.662(5)	−0.9223(223)	−0.06736(1956)		5.308
1.35	4.695(7)	−1.295(67)	0.7986(1469)	−0.5310(893)	1.011
2.07	5.174(2)	−0.8904(40)			9.161
2.07	5.177(4)	−0.9056(177)	0.01356(1531)		10.21
2.07	5.158(6)	−0.7119(432)	−0.4381(932)	0.2819(574)	8.220

Table 4.3: Coefficients of polynomial series for S_p^3, S_p^5, and S_p^7.

factor at $\mu/T \lesssim 0.6$. Meanwhile, the result of g_F^2 is consistent with the previous lattice result up to $\mu/T \lesssim 0.8$. In the previous study, n_q is described by a polynomials of μ/T up to the third order. We then expand the hyperbolic sine function into a polynomial series μ/T up to the third order, and denote the function by $\bar{g}_F^2$. This is represented by a pair of dotted lines. Again, two lines mean the upper and lower bounds of $\bar{g}_F^2$. This result is consistent with the previous lattice results. The difference between g_F^2 and $\bar{g}_F^2$ at $\mu/T \gtrsim 0.9$ comes from the contribution higher than $(\mu/T)^3$. Therefore, the result of g_F^2 is reliable at least at $\mu/T \lesssim 0.9$.

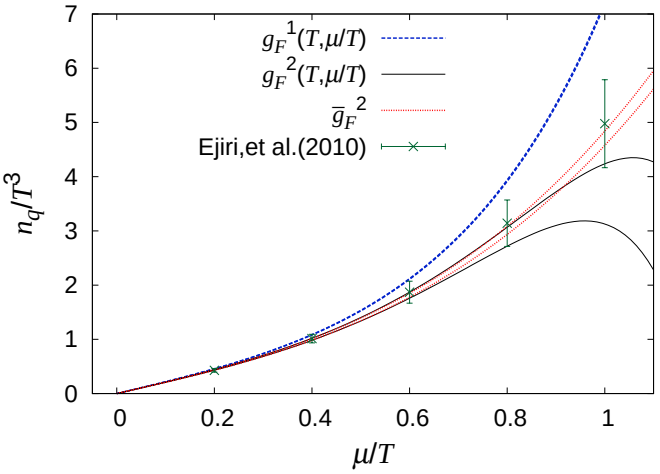

Figure 4.5: μ/T dependence of n_q/T^3 at $T = 0.99T_c$.

Figure 4.6 shows μ/T dependence of n_q/T^3 at $T = 0.93T_c$. The definition of lines is the same as in Fig. 4.5. The difference between of g_F^1 and g_F^2 becomes small as T decreases from $T = 0.99T_c$ to $0.93T_c$. This means that the higher-order contributions become less important as T decreases. Thus the extrapolation by g_F^2 is reliable at $\mu/T \lesssim 0.9$ for $T = 0.93T_c$, because for $T = 0.99T_c$ the extrapolation by g_F^2 is reliable at least at $\mu/T \lesssim 0.9$.

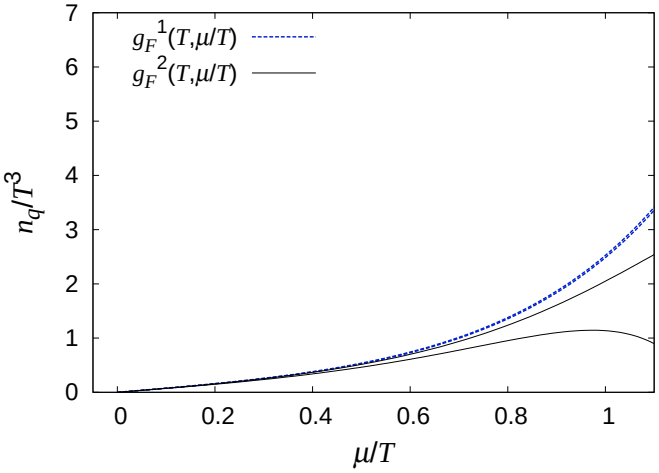

Figure 4.6: μ/T dependence of n_q/T^3 at $T = 0.93T_c$.

Figures 4.7, 4.8 and 4.9 show μ/T dependence of n_q/T^3 at $T = 1.20T_c$, $1.35T_c$ and $2.07T_c$, respectively. The previous LQCD results [29] are represented by green symbols with error bars. A pair of dashed (solid) lines represent the results of g_p^3 (g_p^5). Again, a pair of same lines mean the upper and lower bounds of the extrapolation. The bounds of g_p^3 stem from the errors of $a_p^{(1)}$ and $a_p^{(3)}$, while those of g_p^5 come from the errors of $a_p^{(1)}$, $a_p^{(3)}$ and $a_p^{(5)}$. For each case, the result of g_p^3 is consistent with the previous lattice result [29]. This is natural, because we consider the polynomial series of μ/T up to the third order in both the present and previous studies. Moreover, the difference between g_p^3 and g_p^5 becomes smaller in a range of $\mu/T = 0 \sim 1$ as T increases. This means that the higher-order contributions of the polynomial series become less important as T increases.

Now we consider the upper bound $(\mu/T)_{\max}$ of reliable extrapolation region for $T > T_{\rm RW}$. In order to estimate $(\mu/T)_{\max}$, we define the relative difference between g_p^3 and g_p^5 as $\delta \equiv |g_p^5 - g_p^3|/g_p^5$. Then we assume that the extrapolation is reliable if $\delta < 0.1$.

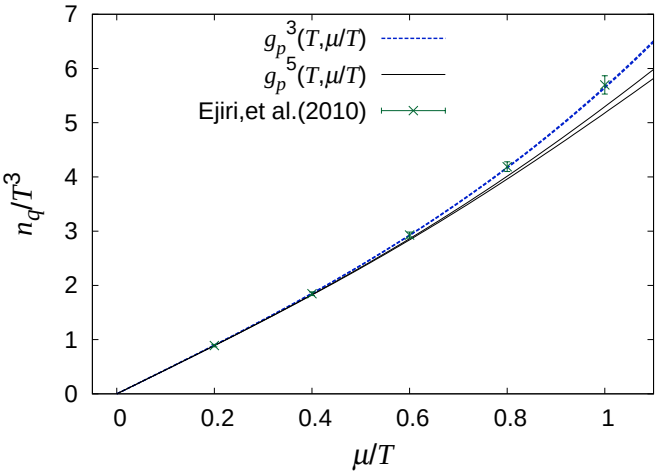

Figure 4.7: μ/T dependence of n_q/T^3 at $T = 1.20T_c$.

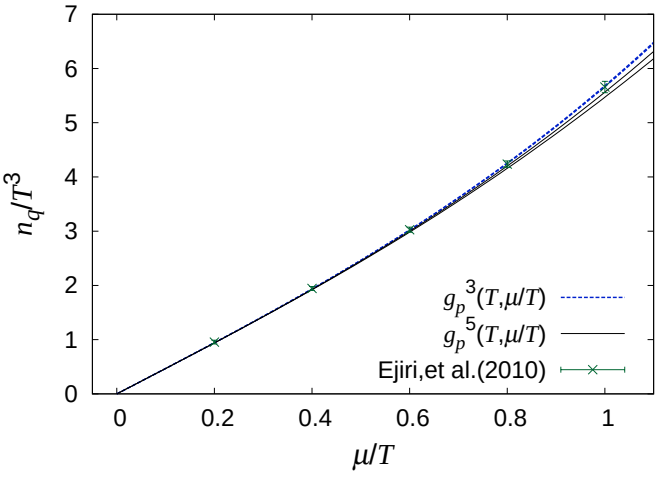

Figure 4.8: μ/T dependence of n_q/T^3 at $T = 1.35T_c$.

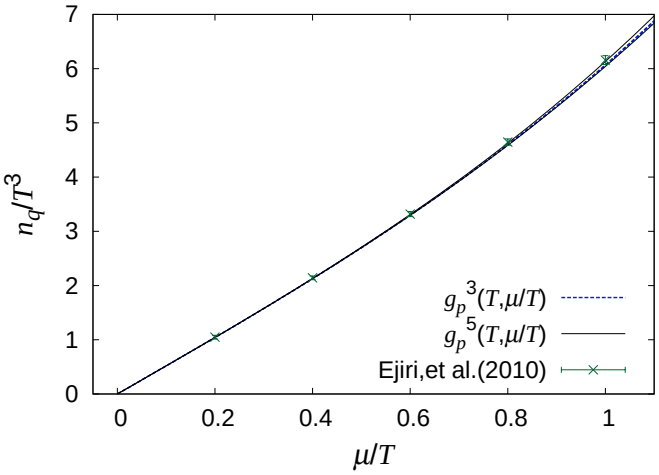

Figure 4.9: μ/T dependence of n_q/T^3 at $T = 2.07T_c$.

The relative differences exceed 10 % at $\mu/T \simeq 0.72$ for $T = 1.20T_c$, $\mu/T \simeq 1.2$ for $T = 1.35T_c$ and $\mu/T \simeq 2.6$ for $T = 2.07T_c$, as shown by the vertical dotted line in Fig. 4.10. Figure 4.11 shows the upper bound $(\mu/T)_{\rm max}$ of the reliable extrapolation as a function of T for the case of $T > T_{\rm RW}$. The upper bound $(\mu/T)_{\rm max}$ goes up as T increases. This indicates that the higher-order contribution becomes less important as T goes up. Thus our present results of g_p^3 and the previous results [29] obtained by using the Taylor expansion method for the reweighting factor become more reliable as T increases.

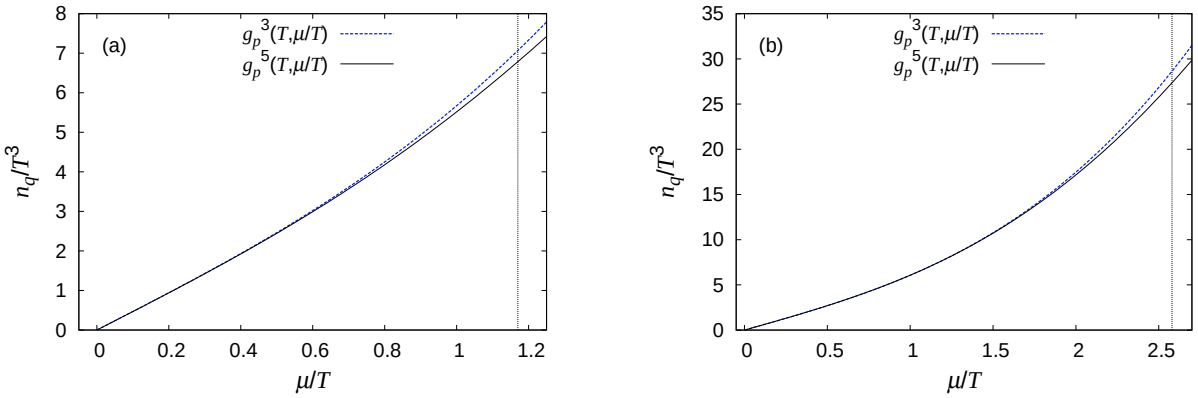

Figure 4.10: Reliable extrapolation region for (a) $T = 1.35T_c$ and (b) $T = 2.07T_c$. The left-hand side of the vertical dotted line shows a reliable extrapolation region with $\delta \leq 0.1$.

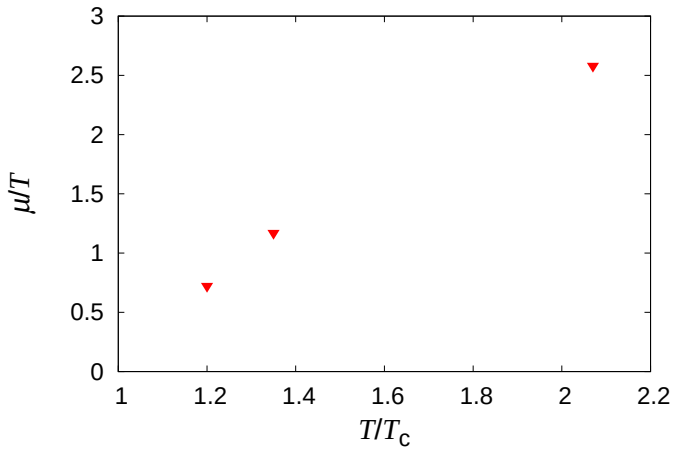

Figure 4.11: Upper bound $(\mu/T)_{\rm max}$ of the reliable extrapolation region as a function of T for the case of $T > T_{\rm RW}$.

4.5 Hadron resonance gas model

In this section, we analyze our lattice results at imaginary μ and $T < T_{\rm c}$ by using the hadron resonance gas (HRG) model. The HRG model is often used to extract baryon masses [73] and thermodynamic properties at $\mu = 0$ [77, 78] and at $\mu \neq 0$ [79]. In Refs. [77, 79], the HRG model well reproduces LQCD results on pressure, energy density and/or number susceptibility at $T < 1.2T_{\rm c}$. This means that the HRG model is applicable for n_q at imaginary μ when we consider the confinement region. Therefore we assess whether baryon masses can be deduced from our LQCD data on n_q at imaginary μ by using the HRG model.

The HRG model is constructed by free hadrons and resonances, each with species i of mass m_i, baryon number B_i and isospin I_{3i}:

$$p^{\rm HRG} = -\frac{T}{V}\sum_{i\in{\rm meson}} \ln Z_i^M(T,V,\mu_i) - \frac{T}{V}\sum_{i\in{\rm baryon}} \ln Z_i^B(T,V,\mu_i) \qquad (4.8)$$

for

$$\ln Z_i^{\mathrm{M/B}} = \pm \frac{V g_i}{2\pi^2} \int_0^\infty dp p^2 \ln\left(1 + z_i e^{-\epsilon_i/T}\right) \tag{4.9}$$

with energies $\epsilon_i = \sqrt{p^2 + m_i}$, degeneracy factors g_i and fugacities

$$z_i = e^{\mu_i/T} = \exp\left(\frac{B_i \mu_{\mathrm{B}} + 2I_{3i}\mu_{\mathrm{iso}}}{T}\right), \tag{4.10}$$

where $\mu_{\mathrm{B}}(\equiv 3\mu)$ is the baryon chemical potential and μ_{iso} is the isospin chemical potential. Here, we do not consider the isospin chemical potential: $\mu_{\mathrm{iso}} = 0$. The baryon number density is easily obtained by

$$n_{\mathrm{B}}^{\mathrm{HRG}} = -\frac{\partial}{\partial \mu_{\mathrm{B}}} p^{\mathrm{HRG}}. \tag{4.11}$$

LQCD simulations have lattice artifacts, as discussed in Refs. [30, 29, 73, 80, 81]. For example, when the number of N_t is small, thermodynamic quantities exceed the Stefan-Boltzmann (SB) limit. It is difficult for finite-T simulations to eliminate the lattice artifacts. We then take the following remedy in this study. We consider the lattice SB limit which is calculated by the lattice action with massless and free quarks, and divide our lattice results by the lattice SB limit. Thus, we regard this normalized value as a lattice-artifact-reduced quantity. In Appendix B, the lattice SB limit is explained for the quark number density. For the HRG model, the quark number density is divided by the continuum SB limit. Then, we compare the lattice results with the HRG results. In the HRG model, we assume that the nucleon masses m_N and the Δ-resonance mass m_Δ depend only on T, and consider that 24 resonance states above the mass threshold $m_{\mathrm{cut}}^{\mathrm{B}}$ have a common mass 1.8 GeV, following Ref. [73]. However note that the contribution of 24 resonance states to n_q is small.

Figure 4.12 shows θ dependence of the normalized quark number density n_q/n_{SB} at $T = 0.93T_{\mathrm{c}}$ and $0.99T_{\mathrm{c}}$. The symbols with error bars represent LQCD results, while the solid lines denote the HRG results. The HRG results well reproduce the lattice results for each temperature. This implies that m_N and m_Δ hardly depend on θ. The resulting nucleon and Δ-resonance masses are summarized for each temperature in Table 4.4, together with χ^2/dof values. We obtain masses heavier than the physical

masses, because the quark mass is much heavier than the physical value in our simulations. As shown in Table 4.12, both m_N and m_Δ decrease by about 10%, when temperature increases from $0.93T_c$ to $0.99T_c$. Thus, we can deduce baryon masses at finite T from θ dependence of $n_q/n_{\rm SB}$ calculated by LQCD.

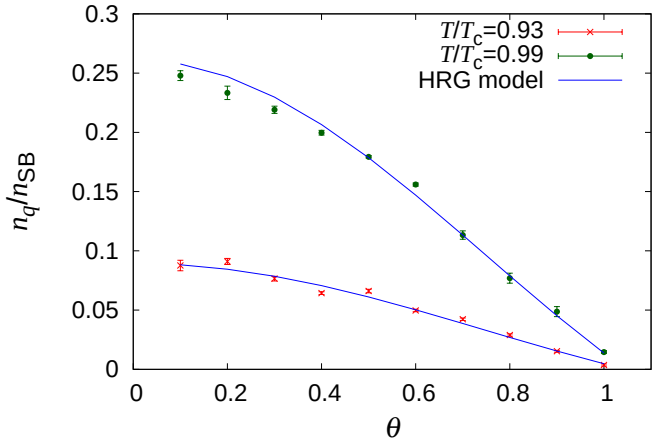

Figure 4.12: θ dependence of $n_q/n_{\rm SB}$ at $T = 0.93T_c$ and $0.99T_c$.

T/T_c	m_N	m_Δ	χ^2/dof
0.93	1091 MeV	1547 MeV	6.625
0.99	940 MeV	1385 MeV	7.993

Table 4.4: Results of χ^2 fitting for m_N and m_Δ in the HRG model and χ^2/dof at $T = 0.93T_c$ and $0.99T_c$.

Finally we consider $n_q/n_{\rm SB}$ in the real μ region at $T = 0.99T_c$. Figure 4.13 shows μ/T dependence of $n_q/n_{\rm SB}$ at $T = 0.99T_c$. The symbols with error bars and the solid line represent the results of Ref. [29] and the result of the HRG model at $T = 0.99T_c$, respectively. The m_N and m_Δ determined at imaginary μ are used in the HRG model to calculate $n_q/n_{\rm SB}$ at real μ, while the previous LQCD results were calculated with the Taylor expansion method for the reweighting factor. The HRG result is consistent with the LQCD results at $\mu/T < 0.4$. Beyond the range, the HRG result overestimates the LQCD results. Thus, the HRG model is reliable only at small μ, when μ is real.

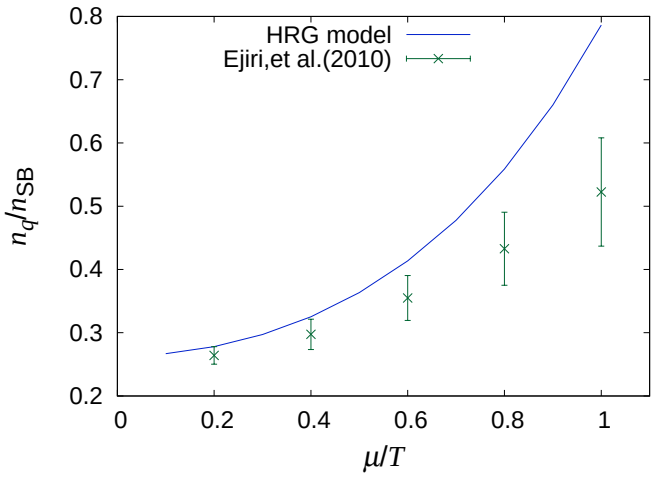

Figure 4.13: μ/T dependence of $n_q/n_{\rm SB}$ at $T = 0.99T_{\rm c}$.

4.6 Short summary

We have researched μ dependence of n_q in both the imaginary and real μ regions. LQCD simulations were performed at imaginary μ on a $8^2 \times 16 \times 4$ lattice with the two-flavor clover-improved Wilson quark action and the renormalization-group-improved Iwasaki gauge action. We considered two temperatures below $T_{\rm c}$ and four temperatures above $T_{\rm c}$. The quark number density was computed along the line of constant physics at $m_{\rm PS}/m_{\rm V} = 0.80$. At imaginary μ, the quark number densities were expanded up to the fourth order of $\theta(= \mu_{\rm I}/T)$, and then extrapolated to real μ by replacing $i\mu_{\rm I}/T$ with $\mu_{\rm R}/T$.

First, we have confirmed with the Wilson-type fermion action that the RW transition takes place at least at $T = 2.07T_{\rm c}$. The quark number density obtained at imaginary μ is consistent with the previous results [39] calculated with the staggered-type quark action. For the quark number density, the LQCD results are thus independent of fermion action taken.

We obtained the quark number density at real μ by extrapolating the results from imaginary to real μ by using the Fourier series g_F^n for $T < T_{\rm c}$ and the polynomial series g_p^{2n-1} for $T > T_{\rm RW}$. As for $T = 0.99T_{\rm c}$, the result of g_F^2 is consistent with the previous results [29] calculated with the Taylor expansion method for the reweighting factor in a range of $\mu/T \lesssim 0.9$. Thus the extrapolation is reliable at $\mu/T \lesssim 0.9$ for $T = 0.99T_{\rm c}$. Moreover, the difference between the results of g_F^1 and g_F^2 becomes small

when T goes down from $T = 0.99T_{\rm c}$ to $0.93T_{\rm c}$. This means that the higher-order contributions become less important as T decreases. The extrapolation by g_F^2 is thus reliable at $\mu/T \lesssim 0.9$ for any T less than $T_{\rm c}$.

As for $T > T_{\rm RW}$, the result of g_p^3 is consistent with the previous results [29] calculated with the Taylor expansion method for the reweighting factor. We estimated the upper bound $(\mu/T)_{\rm max}$ of the reliable extrapolation region of g_p^3. The upper bound $(\mu/T)_{\rm max}$ goes up as T increases. This indicates that the higher-order contributions becomes less important as T increases.

We have analyzed μ dependence of the quark number density at imaginary and real μ by using the HRG model. In Refs. [77, 79], the HRG model well reproduces LQCD results on thermodynamic quantities as $T < 1.2T_{\rm c}$. This means that the HRG model is applicable for n_q at imaginary μ for $T < T_{\rm c}$. Therefore we assessed whether T dependence of baryon masses can be deduced from LQCD data on n_q at imaginary μ by using the HRG model. The HRG results well reproduce the lattice results at imaginary μ when both m_N and m_Δ depend on T only. This implies that m_N and m_Δ hardly depend on $\theta(= \mu_{\rm I}/T)$. Both m_N and m_Δ decrease by about 10% when T increases from $T = 0.93T_{\rm c}$ to $0.99T_{\rm c}$. We propose this method as a practical way of determining T dependence of m_N and m_Δ in the vicinity of $T_{\rm c}$, since it is not easy to evaluate the masses directly with LQCD simulations.

Chapter 5

Summary

In this dissertation, we have investigated the static-quark free energy and the quark number density at finite T and μ by using LQCD with two-flavor Wilson fermions, as the first step toward our final goal of understanding the QCD phase diagram. There are many interesting topics on QCD at finite μ; for example, the inner-core structure of compact stars, the beam energy scan experiments of the QCD phase diagram, and many trials of first-principle calculations. The static-quark free energy characterizes the interaction between quarks in QGP, and the quark number density is a fundamental quantity to study high-density physics. LQCD is the first-principle calculation of QCD, but it has the notorious sign problem at finite μ. In this study, we then took the imaginary-μ approach as a method to avoid the sign problem. It is significant to study μ dependence of the static-quark free energy and the quark number density by using the imaginary-μ approach from the viewpoint of not only physical interest but also consistency check between different methods and quark actions.

We have studied μ dependence of the static-quark free energies in both the imaginary and real μ regions. LQCD simulations were performed at imaginary μ on a $16^3 \times 4$ with the clover-improved two-flavor Wilson fermion action and the renormalization-group-improved Iwasaki gauge action. The static-quark free energy at imaginary μ was expanded up to the fourth order of $\theta(= \mu_{\rm I}/T)$, and the expansion form was extrapolated to real μ by replacing $i\theta$ with $\mu_{\rm R}/T$. We found that the fourth-order term weakens $(\mu/T)^2$ dependence of the static-quark free energy at real μ. This indicates that the contribution is not negligible. At large distances, the static-quark free energies in all the color channels tend to twice the single-quark free energy in the case

of finite μ as well as the case of finite T and zero μ [26]. For both imaginary and real μ, the static-quark free energies are attractive in the color-singlet and -antitriplet channels but they are repulsive in the color-octet and -sextet channels. In order to analyze color screening effects for finite μ, we have investigated μ dependence of the color-Debye screening mass in both the imaginary and the real μ region. The color-Debye screening mass m_D was extracted from LQCD data on the static-quark free energies at imaginary μ by assuming the screened Coulomb form, and the Coulomb form was extrapolated to real μ by expanding it with respect to θ up to the second order and replacing $i\theta$ by $\mu_{\rm R}/T$. As for m_D/T, our results are bigger than the HTLpt predictions in magnitude and stronger in $(\mu/T)^2$ dependence.

We have studied the quark number density n_q in both the imaginary and real μ regions. LQCD simulations were performed at imaginary μ on a $8^2 \times 16 \times 4$ with the clover-improved two-flavor Wilson fermion action and the renormalization-group-improved Iwasaki gauge action. The n_q obtained at imaginary μ are consistent with the previous results [39] calculated with the staggered-type quark action. We obtained n_q at real μ by extrapolating the results from imaginary to real μ by using the Fourier series g_F^n for $T < T_{\rm c}$ and the polynomial series g_p^{2n-1} for $T > T_{\rm RW}$. As for $T = 0.99T_{\rm c}$ at real μ, the resulting function g_F^2 is consistent with the previous results [29] of the Wilson-type quark action based on the Taylor expansion method for the reweighting factor in the range of $\mu/T \lesssim 0.9$. As for $T > T_{\rm RW}$ at real μ, the results of g_p^3 are consistent with the previous results [29]. The upper bound $(\mu/T)_{\rm max}$ of the reliable extrapolation region of g_p^3 goes up as T increases. The HRG model is reliable in the confinement region. Therefore, we have analyzed n_q at $T < T_{\rm c}$. The HRG results well reproduce the lattice results at imaginary μ when both m_N and m_Δ depend on T only, and both m_N and m_Δ decrease by about 10% when T increases from $T = 0.93T_{\rm c}$ to $0.99T_{\rm c}$.

In conclusion, the imaginary-μ approach works well for the static-quark free energies and the quark number density in two-flavor LQCD with the clover-improved Wilson quark action. Our results agree with the previous results at both imaginary and real μ. In addition, we proposed an accessible way of determining T dependence of m_N and m_Δ in the vicinity of $T_{\rm c}$. This way is quite practical, since it is not easy to measure baryon pole masses at finite T directly with LQCD simulations.

Acknowledgments

First of all I would like to express my special gratitude to Prof. Masanobu Yahiro. He guided me to physics of QCD which is curious and interesting, and always helped and supported my research as a supervisor. In addition, he understood that I got a job at the Japan Meteorological Agency(JMA) in the middle of Doctor's Course and supported my management of my job and research at the same time.

I really appreciate Prof. Hiroaki Kouno, Prof. Atsushi Nakamura, Assistant Prof. Takuya Saito and Dr. Keitaro Nagata. They gave me a lot of useful comments and helpful discussions on my research. I have been able to obtain much beneficial knowledge from all the discussions with them. Especially, I owe my great work of lattice QCD entirely Prof. Nakamura's teaching.

I would like to thank Associate Prof. Yoshifumi R. Shimizu, Assistant Prof. Takuma Matsumoto, Prof. Kenzo Inoue, and Associate Prof. Kazuyuki Ogata for useful comments about nuclear physics and elementary particle physics in all the seminars and their lessons. I am thankful to all the members of theoretical nuclear physics and elementary particle physics, and my friends in other divisions in Kyushu University. I would like to thank Assistant Prof. Jun Matsui for his helpful comments in the Front Researcher Development program. I feel truly grateful to Yuki Yamaji, Yuko Megumi, Saori Shigematsu, Hiromi Tsuchijima, Megumi Ieda, Noriko Taguchi, and Mayumi Takaki for their practical supports.

This work was supported by the Research Fellowship of the Japan Society for the Promotion of Science(JSPS) for Young Scientists (grant no. 25-3944), and the numerical calculations were performed on NEC SX-9 and SX-8R at CMC, Osaka University and on HITACHI HA8000 at Research Institute for Information Technology, Kyushu University.

I would like to express my appreciation to the JMA. The JMA permitted me to

work though I was a student of Doctor's Course.

Finally I would like to thank my family for a lot of supports and encouragements. Without their supports I could not have accomplished this great work.

Appendix A

Gauge fixing on the lattice

When the static-quark free energy is calculated in each color channel from the correlator of Polyakov loop operator, the gauge fixing is necessary because this free energy is gauge-variant as shown in Eqs. (3.2)-(3.5). In this appendix, we explain the Coulomb gauge fixing on a lattice, following Ref. [82] where the Landau gauge fixing is explained.

A.1 Basic idea

In the continuum limit, the Coulomb gauge is defined by

$$\partial_\nu A^\nu(x) = 0, \tag{A.1}$$

where the index ν takes over $\nu = 1, 2, 3$ [1]. This condition can be considered as a global variational problem of minimizing the integral

$$\delta \left(\int d^4x A_\nu A^\nu \right) = 0. \tag{A.2}$$

This form can be translated into the lattice formulation as follows. If the function

$$F(G) \equiv \mathrm{Re} \left[\mathrm{tr_c} \sum_\nu \sum_x U_\nu^{(G)}(x) \right] \tag{A.3}$$

[1] In the Landau gauge, the index ν takes over $\nu = 1, 2, 3, 4$.

becomes either minimum or maximum, both the minimizing and maximizing $F(G)$ will satisfy the condition (A.1), where tr_c represents the trace in color space and the $U_\nu^{(G)}$ are link variables after the local gauge transformation by using the matrices G in the gauge group $SU(3)$,

$$U_\nu(x) \longrightarrow U_\nu^{(G)}(x) = G(x)U_\nu(x)G^\dagger(x+\hat{\nu}). \tag{A.4}$$

The gauge fixing on the lattice is then achieved by the maximizing or minimizing $F(G)$.

A lot of methods were proposed so far for actual construction of Eq. (A.3) from the viewpoint of calculation speed. Here we consider the "Los Alamos method" [83] as a gauge-fixing procedure. Let us define the function $w(x)$ as

$$w(x) = \sum_\nu \left(U_\nu(x) + U_\nu^\dagger(x-\hat{\nu}) \right). \tag{A.5}$$

Equation (A.3) is then rewritten into

$$F(G) = \frac{1}{2}\mathrm{Re}\left[\mathrm{tr_c} \sum_x \sum_\nu \left(U_\nu^{(G)}(x) + U_\nu^{(G)\dagger}(x-\hat{\nu}) \right) \right] \tag{A.6}$$

$$= \frac{1}{2}\mathrm{Re}\left[\mathrm{tr_c} \sum_{x \in \text{odd or even site}} w^{(G)}(x) \right] \tag{A.7}$$

where in Eq. (A.7) the summation works at odd (even) sites when the iteration number is odd (even). By this prescription, the gauge transformation becomes

$$U_\nu(x) \rightarrow G(x)U_\nu(x)\mathbf{1}, \tag{A.8}$$

$$U_\nu(x-\hat{\nu}) \rightarrow \mathbf{1}U_\nu(x-\hat{\nu})G^\dagger(x), \tag{A.9}$$

and can be carried out in parallel on a lattice. This iterative step can be reconstructed into the simple form,

$$w(x) \rightarrow w^{(G)}(x) = G(x)w(x). \tag{A.10}$$

The construction of $G(x)$ is explained in the next section.

A.2 Techniques

A.2.1 Reunitarization

A proper unitarization is necessary for the $U_\nu(x)$, when they are gauge-transformed iteratively to construct both the maximizing and minimizing $F(G)$. In the Los Alamos method, the maximal-trace-projection method based on the Cabibbo-Marinari trick [84] is used. In this method, $G(x)$ is computed iteratively:

$$G^i(x) \longrightarrow G^{i+1}(x) = A_1^i A_2^i A_3^i, \tag{A.11}$$

$$G^0(x) = w(x), \tag{A.12}$$

where the subscript i denotes the i-th step of iteration and

$$A_1^i = \begin{pmatrix} \tilde{G}_{11}^{i*} + \tilde{G}_{22}^i & -\tilde{G}_{12}^i + \tilde{G}_{21}^{i*} & 0 \\ \tilde{G}_{12}^{i*} - \tilde{G}_{21}^i & \tilde{G}_{11}^i + \tilde{G}_{22}^{i*} & 0 \\ 0 & 0 & 1 \end{pmatrix}, \tag{A.13}$$

$$A_2^i = \begin{pmatrix} \tilde{G}_{11}^{i*} + \tilde{G}_{33}^i & 0 & -\tilde{G}_{13}^i + \tilde{G}_{31}^{i*} \\ 0 & 1 & 0 \\ \tilde{G}_{13}^{i*} - \tilde{G}_{31}^i & 0 & \tilde{G}_{11}^i + \tilde{G}_{33}^{i*} \end{pmatrix}, \tag{A.14}$$

$$A_3^i = \begin{pmatrix} 1 & 0 & 0 \\ 0 & \tilde{G}_{22}^{i*} + \tilde{G}_{33}^i & -\tilde{G}_{23}^i + \tilde{G}_{32}^{i*} \\ 0 & \tilde{G}_{23}^{i*} - \tilde{G}_{32}^i & \tilde{G}_{22}^i + \tilde{G}_{33}^{i*} \end{pmatrix}. \tag{A.15}$$

The $\tilde{G}_{mn}^i$ represent the G_{mn}^i normalized by the scale factor N_k^i, where the G_{mn}^i are elements of $G(x)$ and the scale factors N_k^i are defined as

$$N_1^i = \sqrt{|G_{11}^{i*} + G_{22}^i|^2 + |G_{21}^{i*} + G_{12}^i|^2}, \tag{A.16}$$

$$N_2^i = \sqrt{|G_{11}^{i*} + G_{33}^i|^2 + |G_{31}^{i*} + G_{13}^i|^2}, \tag{A.17}$$

$$N_3^i = \sqrt{|G_{22}^{i*} + G_{33}^i|^2 + |G_{32}^{i*} + G_{23}^i|^2}. \tag{A.18}$$

The maximal step is about $i = 6$, and we use G^i as $G(x)$ in Eq. (A.10).

A.2.2 Convergence criteria

The quality of gauge fixing is estimated by $\delta = |\mathrm{Ext}(F) - F_i|$, where $\mathrm{Ext}(F)$ means the extreme value of $F(G)$. Since the extreme value of $F(G)$ is unknown during iteration, we judge it by the condition of

$$\sigma = \frac{1}{N_c N_V} \sum_x \mathrm{tr}_c(\partial_\mu A^\mu)(\partial_\mu A^\mu)^\dagger \simeq 0, \tag{A.19}$$

where N_c is the number of colors and N_V is the lattice volume.

A.2.3 Stochastic overrelaxation

For the iteration procedure of Eq. (A.11), some methods were proposed to accelerate convergence of δ. We use the method of stochastic overrelaxation [83]. In this method, $G^2(x)$ is applied with probability p instead of $G(x)$ during the gauge transformation. The value σ diverges for $p = 1$, but rarely diverges for $p < 1$. It is found in Ref. [82] that σ converges relatively quickly, compared with other methods such as the Fourier acceleration method [85] and the overrelaxation method [86].

Appendix B

Wilson fermion in the massless free gas limit

In this appendix, we explain the Wilson fermion in the lattice Stefan-Boltzmann (SB) limit, that is to say, in the massless free gas limit on a lattice. In Sec. 4.5, we consider $n_{\rm SB}$ in order to reduce lattice artifacts. One of the lattice artifacts is due to the coarse lattice. The quark number density n_q in the continuum SB limit is calculated to

$$\frac{n_{\rm SB}}{T^3} = \frac{g}{6}\left[\frac{\mu}{T} + \frac{1}{\pi^2}\left(\frac{\mu}{T}\right)^3\right], \tag{B.1}$$

where g is the degeneracy factor, but our results with $N_t = 4$ lattice overestimate results of Eq. (B.1), as shown in Fig. 4.2. This shows that lattice artifacts exist. Therefore, we have to consider the SB limit on a discretized space-time. In Appendix of Ref. [29], the lattice SB limit is discussed for Wilson fermions, and the pressure and the second-order coefficient of the Taylor expansion at $\mu = 0$ are calculated in the limit, but the quark number density is not.

In the high-T limit, quarks become massless and non-interacting particles, since the quark mass and the gauge coupling are negligibly small compared with T. This situation corresponds to $U_\mu(x) = 1$ in the lattice formulation. Therefore, the partition function with free Wilson fermions is given by

$$Z(\kappa, \hat{\mu}) \;=\; (\det M)^{N_f}, \tag{B.2}$$

$$
\begin{aligned}
M_{xy} &= \delta_{xy} - \kappa \sum_{i=1}^{3} \left[(1-\gamma_i)\delta_{x+\hat{i},y} + (1+\gamma_i)\delta_{x-\hat{i},y} \right] \\
&\quad -\kappa \left[e^{+\hat{\mu}}(1-\gamma_4)\delta_{x+\hat{4},y} + e^{-\hat{\mu}}(1+\gamma_4)\delta_{x-\hat{4},y} \right], \qquad \text{(B.3)}
\end{aligned}
$$

on an $N_x \times N_y \times N_z \times N_t$ lattice, where $\hat{\mu}$ is the quark-number chemical potential in lattice unit. We perform a unitary transformation to momentum space:

$$
\tilde{M}_{pq} \equiv \frac{1}{N_V} \sum_{x,y} e^{-ipx+iqy} M_{xy} \equiv U^{\dagger}_{px} M_{xy} U_{yq}, \qquad \text{(B.4)}
$$

where

$$
\begin{aligned}
&U_{yq} \equiv \frac{1}{\sqrt{N_V}} e^{iqy}, \quad U^{\dagger}_{px} \equiv \frac{1}{\sqrt{N_V}} e^{-ipx}, \\
&U^{\dagger}_{px} U_{yq} = \frac{1}{N_V} \sum_{x} e^{ix(q-p)} = \delta_{pq}, \quad \det(U^{\dagger}U) = 1. \qquad \text{(B.5)}
\end{aligned}
$$

We then calculate the partition function,

$$
Z(\kappa, \hat{\mu}) = (\det M)^{N_f} = (\det \tilde{M})^{N_f} \qquad \text{(B.6)}
$$

with

$$
\begin{aligned}
\tilde{M}_{pq} &= \frac{1}{N_V} \sum_{x} \Bigg[e^{-ix(p-q)} \Bigg[1 - \kappa \sum_{i=1}^{3} \left\{ (1-\gamma_i) e^{iq_i} + (1+\gamma_i) e^{-iq_i} \right\} \\
&\qquad -\kappa \left\{ e^{+\hat{\mu}}(1-\gamma_4) e^{iq_4} + e^{-\hat{\mu}}(1+\gamma_4) e^{-iq_4} \right\} \Bigg] \Bigg] \qquad \text{(B.7)} \\
&= \delta_{pq} \Bigg[1 - \kappa \sum_{i=1}^{3} (2\cos k_i - 2i\gamma_i \sin k_i) \\
&\qquad -\kappa \{ 2\cos(k_4 - i\hat{\mu}) - 2i\gamma_4 \sin(k_4 - i\hat{\mu}) \} \Bigg], \qquad \text{(B.8)}
\end{aligned}
$$

where

$$
k_i = \frac{2\pi j_i}{N_s}, \; j_i = 0, \pm 1, \cdots, N_s/2 \qquad \text{(B.9)}
$$

for the spatial components ($i = x, y, z$) and

$$
k_4 = \frac{2\pi (j_4 + 1/2)}{N_t}, \; j_4 = 0, \pm 1, \cdots, N_t/2 \qquad \text{(B.10)}
$$

for the time component. Introducing a 4×4 matrix defined by $\tilde{M}_{pq} = \delta_{pq}\tilde{M}(k,\kappa,\hat{\mu})$ and using the identity

$$\det(a_0 I + a_1 i\gamma_1 + a_2 i\gamma_2 + a_3 i\gamma_3 + a_4 i\gamma_4) = (a_0^2 + a_1^2 + a_2^2 + a_3^2 + a_4^2)^2, \qquad \text{(B.11)}$$

we can obtain

$$Z(\kappa,\hat{\mu}) = \left(\prod_k \det \tilde{M}(k,\kappa,\hat{\mu})\right)^{N_c N_f} \qquad \text{(B.12)}$$

with

$$\begin{aligned}
\det \tilde{M}(k,\kappa,\hat{\mu}) &= \left[(1-8\kappa)^2 + 8\kappa(1-8\kappa)\left\{\sum_{i=1}^{3}\sin^2\left(\frac{k_i}{2}\right) + \sin^2\left(\frac{k_4 - i\hat{\mu}}{2}\right)\right\}\right. \\
&\quad +4\kappa^2\left[\left\{2\sum_{i=1}^{3}\sin^2\left(\frac{k_i}{2}\right)\right\}^2 + \sum_{i=1}^{3}\sin^2 k_i\right. \\
&\quad \left.\left.+4\left\{2\sum_{i=1}^{3}\sin^2\left(\frac{k_i}{2}\right) + 1\right\}\sin^2\left(\frac{k_4 - i\hat{\mu}}{2}\right)\right]\right]^2. \qquad \text{(B.13)}
\end{aligned}$$

The massless quark limit corresponds to $\kappa = 1/8$. We then obtain the fermion determinant in the massless free gas limit on a lattice as follows:

$$\begin{aligned}
\det \tilde{M}(k,1/8,\hat{\mu}) &= \frac{16}{8^4}\left[\left\{2\sum_{i=1}^{3}\sin^2\left(\frac{k_i}{2}\right)\right\}^2 + \sum_{i=1}^{3}\sin^2 k_i\right. \\
&\quad \left.+4\left\{2\sum_{i=1}^{3}\sin^2\left(\frac{k_i}{2}\right) + 1\right\}\sin^2\left(\frac{k_4 - i\hat{\mu}}{2}\right)\right]^2. \qquad \text{(B.14)}
\end{aligned}$$

Thermodynamic quantities with Wilson fermions are calculated from this partition function in the lattice SB limit.

The quark number density in the lattice SB limit is then obtained as

$$\begin{aligned}
\frac{n_q}{T^3} &= \frac{N_t^3}{N_V}\frac{\partial}{\partial\hat{\mu}}\ln Z(1/8,\hat{\mu}) \\
&= N_c N_f \frac{N_t^3}{N_V}\sum_k \frac{\partial}{\partial\hat{\mu}}\det \tilde{M}(k,1/8,\hat{\mu})\left[\det \tilde{M}(k,1/8,\hat{\mu})\right]^{-1} \qquad \text{(B.15)}
\end{aligned}$$

with

$$\frac{\partial}{\partial\hat{\mu}}\det\tilde{M}(k,1/8,\hat{\mu}) = -\frac{1}{8^2}\left\{2\sum_i \sin^2\left(\frac{k_i}{2}\right)+1\right\} \times(\sinh\hat{\mu}\cos k_t + i\cosh\hat{\mu}\sin k_t). \tag{B.16}$$

The quark number density at imaginary μ is obtained by replacing $\hat{\mu}$ with $i\hat{\mu}_{\rm I}$ in Eqs. (B.15) and (B.16).

Now we consider effects of lattice discretization. Figure B.1 shows N_t dependence of the ratio $n_{\rm latSB}/n_{\rm SB}$ at $\mu/T = 0.1$, where $n_{\rm latSB}$ and $n_{\rm SB}$ are the quark number densities in the lattice and continuum SB limits, respectively. Each $n_{\rm latSB}$ is calculated on lattices with N_s/N_t fixed at 4, where N_s is the spatial lattice size. As N_t increases, the value $n_{\rm latSB}/n_{\rm SB}$ approaches one. This means that $n_{\rm latSB}$ approaches the continuum limit. In addition, the effects of lattice discretization are not negligible for $N_t < 10$, as shown in Fig. B.1.

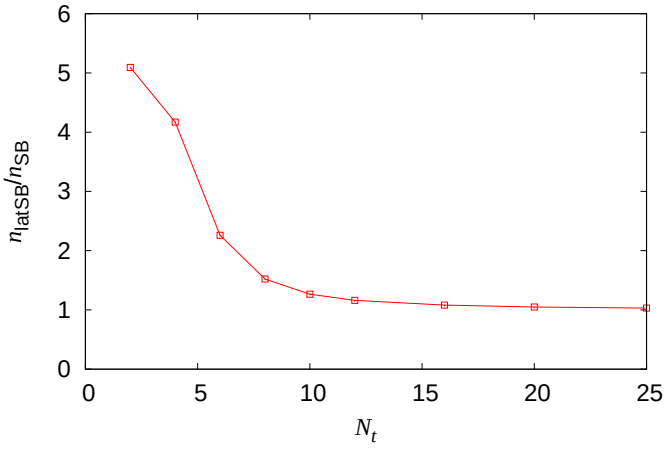

Figure B.1: N_t dependence of ratio $n_{\rm latSB}/n_{\rm SB}$ at $\mu/T = 0.1$.

Bibliography

[1] M. Gell-Mann, Phys. Letters 8, 214 (1964).

[2] J. Beringer, *et al.* (Particle Data Group), Phys. Rev. D 86, 010001 (2012).

[3] S. Aoki, *et al.* (JLQCD Collaboration), Phys. Rev. D 78, 014508 (2008).

[4] B. Svetitsky and Y. Yaffe, Nucl. Phys. B210, 423 (1983).

[5] J. C. Collins and M. J. Perry, Phys. Rev. Lett. 34, 1353 (1975).

[6] S. Aoki, *et al.* (PACS-CS Collaboration), Phys. Rev. D 79, 034503 (2009).

[7] T. Inoue, S. Aoki, T. Doi, T. Hatsuda, Y. Ikeda, N. Ishii, K. Murano, H. Nemura, and K. Sasaki (HAL QCD Collaboration), Phys. Rev. Lett. 111, 112503 (2013).

[8] S. R. Beane, E. Chang, S. Cohen, W. Detmold, H. W. Lin, K. Orginos, A. Parreño, M. J. Savage, and B. C. Tiburzi (NPLQCD Collaboration), Phys. Rev. Lett. 113, 252001 (2014).

[9] Z. S. Brown, W. Detmold, S. Meinel, and K. Orginos, Phys. Rev. D 90, 094507 (2014).

[10] T. Kozik, *et. al.*, Nucl. Phys. A757, 1 (2005).

[11] A. Trzupek, *et. al.*, Nucl. Phys. A757, 28 (2005).

[12] X. L. Wang, *et. al.*, Nucl. Phys. A757, 102 (2005).

[13] O. Zaudkte, *et. al.*, Nucl. Phys. A757, 184 (2005).

[14] Y. Aoki, G. Endrödi, Z. Fodor, S. D. Katz, and K. K. Szabó, Nature (London) 443, 675 (2006).

[15] G. Boyd, J. Engels, F. Karsch, E. Laermann, C. Legeland, M. Lütgemeier, and B. Petersson, Nucl. Phys. B469 (1996) 419.

[16] F. Karsch, E. Laermann, and A. Peikert, Phys. Lett. B 478, 447 (2000).

[17] T. Umeda, S. Ejiri, S. Aoki, T. Hatsuda, K. Kanaya, Y. Maezawa, and H. Ohno, Phys. Rev. D 79, 051501 (2009).

[18] S. Borsányi, G. Endrődi, Z. Fodor, A. Jakovac, S. D. Katz, S. Krieg, C. Ratti, K. K. Szabó, J. High Energy Phys. 1011 (2010) 077.

[19] L. Kumar (STAR Collaboration), Nucl. Phys. A904-A905, 256c (2013).

[20] E. O'Brien (PHENIX Collaboration), Nucl. Phys. A904-A905, 264c (2013).

[21] O. Kaczmarek, F. Karsch, E. Laermann, and M. Lutgemeier, Phys. Rev. D 62, 034021 (2000).

[22] A. Nakamura and T. Saito, Prog. Theor. Phys. 111, 733 (2004).

[23] A. Nakamura and T. Saito, Phys. Lett. B 621, 171 (2005).

[24] O. Kaczmarek and F. Zantow, Phys. Rev. D 71, 114510 (2005).

[25] V. G. Bornyakov *et al.* (DIK Collaboration), Phys. Rev. D 71, 114504 (2005).

[26] Y. Maezawa, N. Ukita, S. Aoki, S. Ejiri, T. Hatsuda, N. Ishii, and K. Kanaya (WHOT-QCD Collaboration), Phys. Rev. D 75, 074501 (2007).

[27] Y. Maezawa, T. Umeda, S. Aoki, S. Ejiri, T. Hatsuda, K. Kanaya, and H. Ohno (WHOT-QCD Collaboration), Prog. Theor. Phys. 128, 955 (2012).

[28] M. Döring, S. Ejiri, O. Kaczmarek, F. Karsch, and E. Laermann, Eur. Phys. J. C 46, 179 (2006).

[29] S. Ejiri *et al.* (WHOT-QCD Collaboration), Phys. Rev. D 82, 014508 (2010).

[30] C. R. Allton, S. Ejiri, S. J. Hands, O. Kaczmarek, F. Karsch, E. Laermann, and C. Schmidt, Phys. Rev. D 68, 014507 (2003).

[31] A. M. Ferrenberg and R. H. Swendsen, Phys. Rev. Lett. 61, 2635 (1988).

[32] Z. Fodor and S. D. Katz, Phys. Lett. B 534, 87 (2002).

[33] K. Nagata and A. Nakamura, J. High Energy Phys. 04 (2012) 092.

[34] C. R. Allton, S. Ejiri, S. J. Hands, O. Kaczmarek, F. Karsch, E. Laermann, Ch. Schmidt, and L. Scorzato, Phys. Rev. D 66, 074507 (2002).

[35] M. D ' Elia, and M.-P. Lombardo, Phys. Rev. D 67, 014505 (2003).

[36] M. D ' Elia, and M.-P. Lombardo, Phys. Rev. D 70, 074509 (2004).

[37] M. D ' Elia F. D. Renzo, and M. P. Lombardo, Phys. Rev. D 76, 114509 (2007).

[38] P. Cea, L. Cosmai, M. D ' Elia, and A. Papa, J. High Energy Phys. 02 (2007) 066.

[39] M. D ' Elia, and F. Sanfilippo, Phys. Rev. D 80, 014502 (2009).

[40] G. Aarts, Phys. Rev. Lett. 102, 131601 (2009).

[41] G. Aarts, L. Bongiovanni, E. Seiler, D. Sexty, and I.-O. Stamatescu, Eur. Phys. J. A 49, 89 (2013).

[42] D. Sexty, Phys. Lett. B 729, 108 (2014).

[43] G. Aarts, E. Seiler, D. Sexty, and I.-O. Stamatescu, Phys. Rev. D 90, 114505 (2014).

[44] M. Cristoforetti, F. DiRenzo, and L. Scorzato, Phys. Rev. D 86, 074506 (2012).

[45] H. Fujii, D. Honda, M. Kato, Y. Kikukawa, S. Komatsu, and T. Sano, J. High Energy Phys. 10 (2013) 147.

[46] G. Parisi and Y.-S. Wu, Sci. Sinica 24 (1981) 483.

[47] E. Witten, "Analytic Continuation Of Chern-Simons Theory," arXiv:1001.2933 [hep-th] (2010).

[48] A. Roberge and N. Weiss, Nucl. Phys. B275, 734 (1986).

[49] K. G. Wilson, Phys. Rev. D 10, 2445 (1974).

[50] K. G. Wilson, Quarks and strings on a lattice, in *New Phenomena in Subnuclear Physics*, ed. A. Zichichi (Plenum Press, New York), Part A, p. 69 (1975).

[51] H. B. Nielsen and M. Ninomiya, Nucl. Phys. B185 (1981) 20; erratum: B195 (1981) 541.

[52] H. B. Nielsen and M. Ninomiya, Nucl. Phys. B193 (1981) 173.

[53] P. Hasenfratz, F. Karsch, Phys. Lett. 125B, 308 (1983).

[54] B. Sheikholeslami and R. Wohlert, Nucl. Phys. B259, 572 (1985).

[55] Y. Iwasaki, Nucl. Phys. B258, 141 (1985).

[56] A. Ali Khan *et al.* (CP-PACS Collaboration), Phys. Rev. D 63, 034502 (2000).

[57] A. Ali Khan *et al.* (CP-PACS Collaboration), Phys. Rev. D 64, 074510 (2001).

[58] I. Pushkina, P. de Forcrand, M. G. Perez, S. Kim, H. Matsufuru, A. Nakamura, I-O. Stamatescu, T. Takaishi, T. Umeda (QCD-TARO Collaboration), Phys. Lett. B 609 265 (2005).

[59] M. Cheng, *et al.*, Eur. Phys. J. C 71, 1564 (2011).

[60] T. Matsui and H. Satz, Phys. Lett. B 178, 416 (1986).

[61] S. Nadkarni, Phys. Rev. D 33, 3738 (1986).

[62] S. Nadkarni, Phys. Rev. D 34, 3904 (1986).

[63] M. Göckeler, R. Horsley, A. Irving, D. Pleiter, P. Rakow, G. Schierholz, and H. Stüben, Phys. Rev. D 73, 014513 (2006).

[64] A. Ipp and A. Rebhan, J. High Energy Phys. 06 (2003) 032.

[65] N. Haque, J. O. Andersen, M. G. Mustafa, M. Strickland and N. Su, Phys. Rev. D 89, 061701(R) (2014).

[66] E. Braaten and A. Nieto, Phys. Rev. Lett. 76, 1417 (1996); Phys. Rev. D 53, 3421 (1996).

[67] P. B. Demorest, T. Pennucci, S. M. Ransom, M. S. E. Roberts, and J. W. T. Hessels, Nature 467, 1081 (2010).

[68] T. Sasaki, N. Yasutake, M. Kohno, H. Kouno, and M. Yahiro, arXiv:1307.0681 [hep-ph] (2013).

[69] J. Sugano, J. Takahashi, M. Ishii, H. Kouno and M. Yahiro, Phys. Rev. D 90, 037901 (2014).

[70] H. Kouno, Y. Sakai, K. Kashiwa, and M. Yahiro, J. Phys. G 36, 115010 (2009).

[71] Y. Sakai, H. Kouno, and M. Yahiro, J. Phys. G 37, 105007 (2010).

[72] Sz. Borsányi, Z. Fodor, C. Hoelbling, S.D. Katz, S. Krieg, C. Ratti, K.K. Szabó, J. High Energy Phys. 1009 (2010) 073.

[73] P. Huovinen, and P. Petreczky, Nucl. Phys. A837, 26 (2010).

[74] H. Kouno, Y. Sakai, K. Kashiwa, and M. Yahiro, J. Phys. G 36, 115010 (2009).

[75] Y. Sakai, K. Kashiwa, H. Kouno and M. Yahiro, Phys. Rev. D 77, 051901 (2008).

[76] Y. Sakai, T. Sasaki, H. Kouno and M. Yahiro, J. Phys. G 39, 035004 (2008).

[77] S. Borsányi (for the Wuppertal-Budapest Collaboration), Nucl. Phys. A904, 270 (2013).

[78] A. Bazavov, *et al.* (HotQCD Collaboration), Phys. Rev. D 90, 094503 (2014)

[79] Sz. Borsányi, G. Endrődi, Z. Fodor, S.D. Katz, S. Krieg, C. Ratti, K.K. Szabó, J. High Energy Phys. 1208 (2012) 053.

[80] O. Philipsen and L. Zeidlewicz, Phys. Rev. D 81, 077501 (2010).

[81] A. Bazavov et al. (HotQCD Collaboration), Phys. Rev. D 85, 054503 (2012).

[82] H. Suman and K. Schilling, arXiv:9306018 [hep-lat] (1993).

[83] Ph. de Forcrand and R. Gupta, Nucl. Phys. B (Proc. Suppl.) 9, 516 (1989).

[84] N. Cabbibo and E. Marinari, Phys. Lett. B 119, 387 (1982).

[85] J.E. Mandula and M. Ogilvie, Phys. Lett. B 248, 156(1990).

[86] C.T.H. Davies, G.G. Batrouni, G.R. Katz, A.S. Kronfeld, G.P. Lepage, K.G. Wilson, P. Rossi and B. Svetitsky, Phys. Rev. D 37, 1581 (1988).